*J. Fluid Mech.* (2009), *vol.* 631, *pp.* 311–342.  
doi:10.1017/S0022112009007046 Printed in the United Kingdom

# Low-dimensional models and performance scaling of a highly deformable fish pectoral fin

M. BOZKURTTAS[1]†, R. MITTAL[1]‡, H. DONG[1]¶, G. V. LAUDER[2] AND P. MADDEN[2]

[1]Department of Mechanical and Aerospace Engineering, The George Washington University, 801 22nd St NW, Washington DC 20052, USA

[2]Organismic and Evolutionary Biology, 26 Oxford St, Harvard University, Cambridge, MA 02138, USA

(Received 29 July 2008 and in revised form 11 March 2009)

The hydrodynamics of a highly deformable fish pectoral fin used by a bluegill sunfish (*Lepomis macrochirus*) during steady forward swimming are examined in detail. Low-dimensional models of the fin gait based on proper orthogonal decomposition (POD) are developed, and these are subjected to analysis using an incompressible Navier–Stokes flow solver. The approach adopted here is primarily motivated by the quest to develop insights into the fin function and associated hydrodynamics, which are specifically useful for the design of a biomimetic, pectoral fin propulsor. The POD analysis shows that the complex kinematics of the pectoral fin can be described by a few (<5) POD modes and that the first three POD modes are highly distinct. The significance of these modes for thrust production is examined by synthesizing a sequence of fin gaits from these modes and simulating the flow associated with these gaits. We also conduct a scale study of the pectoral fin in order to understand the effect of the two key non-dimensional parameters, Reynolds number and Strouhal number, on the propulsive performance. The implications of the POD analysis and performance scaling on the design of a robotic pectoral fin are discussed.

## 1. Introduction

Many fish employ the so-called labriform propulsion mode in which the primary propulsive force is provided by the motion of the pectoral fins (Lighthill 1975). The pectoral fins of such fish exhibit varying degrees of deformability. In particular, fish that live in energetic marine environments such as rivers, streams, littoral zones and coral reefs tend to have fins that generally exhibit higher levels of deformability. Fin deformability adds significantly to the kinematic repertoire of the fins, and it likely enables these fish to perform a large range of propulsive and manoeuvring tasks that are required for survival in these complex aquatic environments. The pectoral fins of fish usually are membranous structures, supported by a number of bony rays (figure 1) that extend from the pectoral girdle to the outer portions of the fins. These rays can rotate about the joints, and the fish can induce motion as well as conformational change in the fin by differential rotation of these rays. In addition to this active

† Present address: Exa Corporation, 55 Network Drive, Burlington, MA 01803, USA
‡ Email address for correspondence: mittal@gwu.edu
¶ Present address: Mechanical and Materials Engineering, Wright State University, Dayton, OH 45435, USA

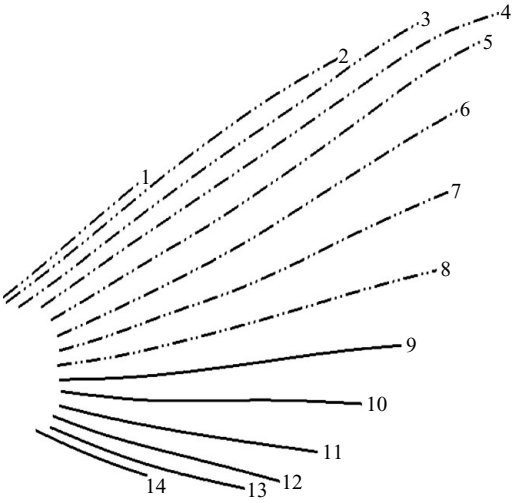


FIGURE 1. Structure of the bluegill pectoral fin which consists of 14 bony rays. A deformable membrane stretches across these rays, and the fin can be actively deformed through angular motion of the rays. The rays are also flexible and allow for passive (flow-induced) bending.

deformation, the fins can also undergo passive deformation due to hydrodynamic loads.

At a rudimentary level, a fish pectoral fin can be considered to be a pitching–rolling (or flapping) foil, and a number of attempts have been made in the past to develop flapping-foil propulsors that can be be used for propulsion and manoeuvring of small underwater vehicles (Triantafyllou, Triantafyllou & Grosenbaugh 1992; Kato & Furushima 1996; Techet *et al.* 2005). One feature that is shared by all these flapping-foil propulsors is that they are quite rigid and not designed to exhibit any significant active or passive deformation. These flapping-foil propulsors also have a few degrees of freedom, which usually include the roll amplitude and the flapping frequency. The use of rigid flapping foils with limited degrees-of-freedom requires relatively simple actuation mechanisms, but in all likelihood, also limits the performance of these propulsors. For instance, recent experimental (Lauder *et al.* 2005, 2006; Lauder & Madden 2006) and numerical studies (Bozkurttas *et al.* 2006; Mittal *et al.* 2006; Dong *et al.* 2009) of the hydrodynamics of labriform swimming in bluegill sunfish with highly deformable pectoral fins have shown that the fin deformation can enable the fish to produce requisite levels of thrust with high efficiency while at the same time limiting the magnitude of the lateral forces that are produced.

The goal of the current study is to gain insights into the kinematics and hydrodynamics of the bluegill sunfish (*Lepomis macrochirus*) pectoral fin that have direct implications for the design and development of a deformable robotic fin propulsor. As will be discussed in the next section, the kinematics of deformable pectoral fins such as those of the sunfish are highly complex and do not lend themselves easily to simple classifications such as 'paddling' or 'flapping' that have been used in the past (Walker & Westneat 1997). A good engineered fin design would be one which is a simple derivation of the fish pectoral fin but one which stills delivers propulsive performance that matches that of the fish fin. This seemingly difficult task would be possible only if one could determine and eliminate features of the fish

fin design and kinematics that contribute to the design complexity but not to the performance of the fin. Since the fin (like most other organs in biological organisms) is not optimized for any single function, it is likely that there are features of the fin and its motion that do not contribute much to the thrust performance. For instance, pectoral fins in fish are not only used for propulsion during steady forward swimming but are also used for manoeuvring, acceleration/deceleration, station keeping and stabilization. In fact, use of these fins extends beyond locomotion into functions such as, but not limited to, courting, threat displays and excavating burrows. Therefore, it is quite possible that some features of the fin and its motion play little, if any, role in steady forward swimming. An approach is therefore needed that would allow us to determine these ineffective features of the fin motion and eliminate them from the engineered fin design.

In the current study, we have used proper orthogonal decomposition (POD) as the basic toolset to answer some of the issues raised above. POD is a powerful method for data analysis, aimed at obtaining low-dimensional, approximate descriptions of a high-dimensional process or dataset (Liang *et al.* 2002; Barber, Ahmed & Shafi 2005). The POD method has been used in many areas including image processing, data compression, process identification and oceanography (Liang *et al.* 2002). POD has also been used to obtain approximate, low-dimensional descriptions of turbulent flows (Berkooz, Holmes & Lumley 1993), structural vibrations and dynamical systems. Principle-component analysis (PCA) has also been used before for understanding the gaits of biological entities (Urtasun *et al.* 2004). In the current study, POD is used to decompose the fin motion into a relatively small set of components. Subsequently, POD is taken a step further by performing computational fluid dynamics (CFD) analyses of the fin gaits synthesized from the POD modes. Flow simulations of the low-dimensional models are carried out and the nonlinear effects associated with the fluid flow on the linearly superposed gaits examined.

A second issue that is important in the design of such propulsors is the scaling of the fin performance with key parameters that define the size/geometry of the fin as well as its operational characteristics such as frequency and flow speed relative to the fin. The second half of the current study therefore focuses on the scaling of the hydrodynamic performance with two important non-dimensional parameters: the fin Reynolds number and the fin Strouhal number.

## 2. Pectoral fin kinematics

The method used to digitize the bluegill sunfish's pectoral fin kinematics during steady forward motion is described in detail in Standen & Lauder (2005). The fin position through time was digitized using high-speed, high-resolution videos from two orthogonal (ventral and lateral) views. The three-dimensional fin geometry was measured by digitizing the ventral and lateral camera views and using the direct linear transform (DLT) algorithm (Hartley & Zisserman 2004) to calculate the spatial coordinates from the digitized points. The points chosen for tracking were all located on the fin rays and were spaced at about 1 mm intervals along the rays. A cubic spline fit was used to reconstruct the ray geometry. The maximum error in the tracked locations of the points estimated from the DLT analysis was about 0.5 mm, and this was confirmed by comparing the actual ray length of the fish fin with that obtained from the DLT analysis. Given the 4 cm length of the longest fin ray, this amounts to about a 1.25 % maximum position error. About 20 time frames and 280 total points per frame were digitized for one individual fish, and figure 2(*a*) shows a surface

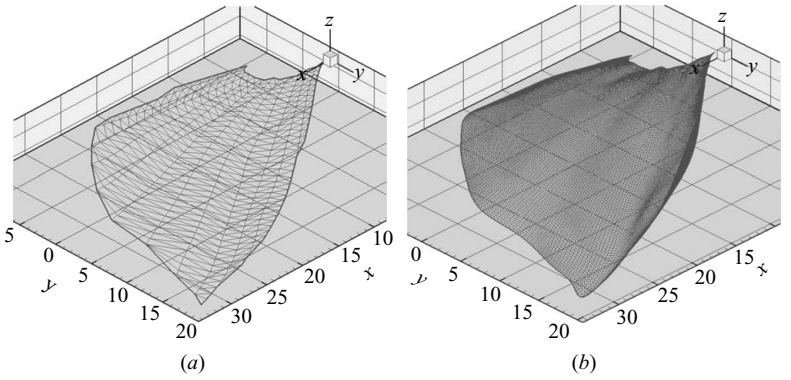


FIGURE 2. (*a*) Surface mesh for the fin constructed from the points tracked in the experiments. (*b*) Finer mesh with triangular elements used in simulations.

mesh constructed from all the (280) points that are tracked on the fin surface at one time instant. This original surface mesh is used as the basis for reconstructing a significantly higher-resolution mesh that is commensurate with the high-resolution fluid mesh used in the simulations. The finer surface mesh employs cubic splines along the ray-to-ray (or chordwise) direction, with the original tracked points on the rays used as the collocation points. This automatically results in the finer surface mesh having a smoother profile in the chordwise direction. Figure 2(*b*) shows this finer mesh which has 34 866 triangular elements. Finally, the 20 time frames are interpolated in time using a cubic spline so as to provide intermediate frames at the much higher frame rate required for CFD.

The fin motion consists of three primary phases; abduction (fin moves away from the body), which extends from $t/\tau = 0$ to about $t/\tau = 0.57$, adduction (fin moves back towards the body), which extends from $t/\tau = 0.57$ to about $t/\tau = 0.96$ and intermediate, which extends from $t/\tau = 0.96$ to $t/\tau = 1.0$. The intermediate phase which is difficult to visualize, is not dynamically significant, since in this phase, the fin is held against the body of the fish and likely does not produce any force during this phase. The abduction and adduction phases are demonstrated in figure 3 via snapshots using two views of the fin-beat cycle. As is clear from figure 3, the fin shows significant deformation during the stroke. The deformation consists of (i) a change in area, (ii) bending in both chordwise and spanwise directions, (iii) distinct correlated movement of the upper (dorsal) and the lower (ventral) edges (while the middle of the fin often lags behind) and (iv) waves of bending that pass out along the fin. This complex motion is difficult to decompose into classical definitions such as 'paddling' or 'flapping'. Furthermore, even if such a decomposition were to be attempted, the applicability of the classical paddling/flapping classification could lead to questionable insights into the hydrodynamics of such fins. For instance, Jayne, Lozada & Lauder (1996) showed that fin kinematics in bass was much more complicated than a rowing model of drag-based propulsion. Ramamurti *et al.* (2002) performed flow simulations of a bird wrasse pectoral fin motion using 14 control points extracted by Walker & Westneat (1997) to describe the fin kinematics. Subsequently, Ramamurti *et al.* (2005) studied the effect of rigidity on the same fin's performance by selecting a further reduced number of control points to define the motion. An approach such as this may have worked for the relatively stiff pectoral fin of the bird wrasse but would be insufficient for the current fin, which undergoes a significantly larger deformation.

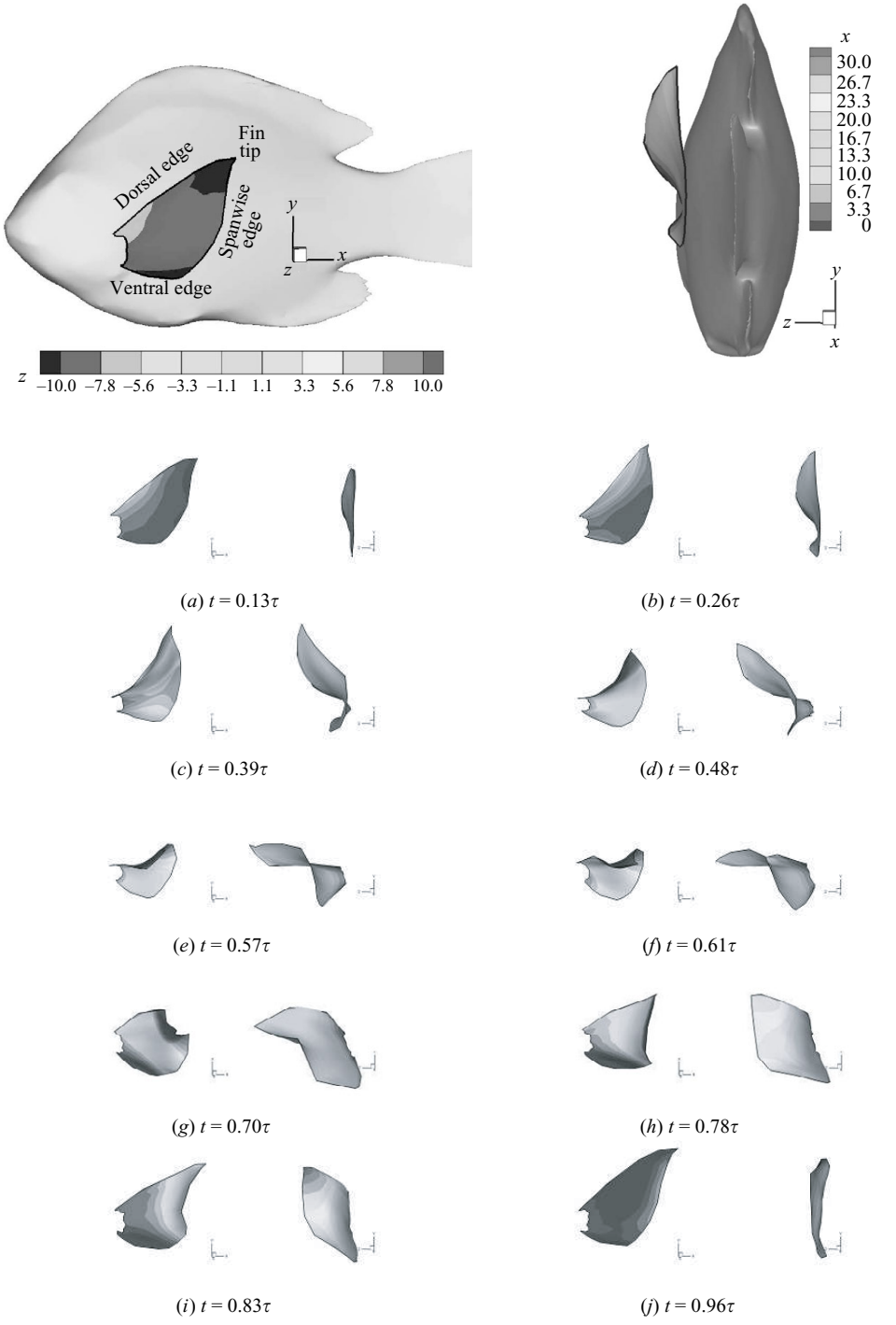


FIGURE 3. Conformation of the sunfish pectoral fin during the fin-beat cycle (of period $\tau$) in steady forward locomotion from side (left) and back (right) views. In side views, shade reflects distance (in mm) from body, and in back views, shades depict distance along the body.

A more inventive approach is therefore needed to decompose and study the motion in a way that would be useful for the design of the deformable robotic pectoral fin. The current paper describes such an approach that makes used of POD coupled with CFD analysis.

## 3. Computational methodology

The simulations employ a sharp-interface immersed-boundary method (Mittal & Iaccarino 2005) that has been described in detail in Dong, Mittal & Najjar (2006) and Mittal *et al.* (2008). The equations governing this flow are the three-dimensional unsteady, viscous incompressible Navier–Stokes equations,

$$\frac{\partial u_i}{\partial x_i} = 0, \tag{3.1a}$$

$$\frac{\partial u_i}{\partial t} + \frac{\partial (u_i u_j)}{\partial x_j} = -\frac{1}{\rho}\frac{\partial p}{\partial x_i} + \nu \frac{\partial}{\partial x_j}\left(\frac{\partial u_i}{\partial x_j}\right), \tag{3.1b}$$

where $u_i$ are the velocity components; $p$ is the pressure; and $\rho$ and $\nu$ are the fluid density and kinematic viscosity, respectively. These equations are discretized using a cell-centred, collocated (non-staggered) arrangement of the primitive variables ($u_i$, $p$). In addition to the cell-centre velocities ($u_i$), face-centre velocities are also computed. Within the context of this method, the cell-centre velocity satisfies the momentum equations, whereas the face-centre velocity satisfies mass conservation (Ye *et al.* 1999). The equations are integrated in time using the fractional step method of Van-Kan (1986).

A multi-dimensional ghost-cell methodology is used to incorporate the effect of the immersed boundary on the flow. This method falls in the category of sharp-interface 'discrete-forcing' immersed-boundary methods as has been described in Mittal & Iaccarino (2005). In the current method, the surface of a three-dimensional body, such as the fish fin, which is the subject of the current study, is represented by an unstructured grid with triangular elements (see figure 2). Using the ghost-cell procedure, the boundary conditions are prescribed to second-order accuracy on the body surface, and this, along with the second-order accurate discretization of the fluid cells, leads to local and global second-order accuracy in the computations. This has been confirmed by simulating flow past a circular cylinder on a hierarchy of grids and examining the error on these grids (Mittal *et al.* 2008).

Boundary motion is accomplished by moving the nodes of the surface triangles in a prescribed manner. The general framework can therefore be considered as Eulerian–Lagrangian, wherein the immersed boundaries are explicitly tracked as surfaces in a Lagrangian mode, while the flow computations are performed on a fixed, Eulerian grid. Further details regarding such immersed-boundary methods can be found in Ye *et al.* (1999), Udaykumar *et al.* (2001) and Mittal & Iaccarino (2005). In addition to the simulations to be presented here, the solver has been validated by simulating flow past stationary as well as accelerating cylinders and spheres. The accuracy of the solver for zero-thickness bodies has been demonstrated by simulating flow past a suddenly accelerated normal plate and comparing results with available experiments and simulations (Mittal *et al.* 2008).

### 3.1. *Simulation set-up*

In this section, we describe the boundary conditions, computational domain and the grids employed in the current simulations. The spanwise length of the fourth ray,

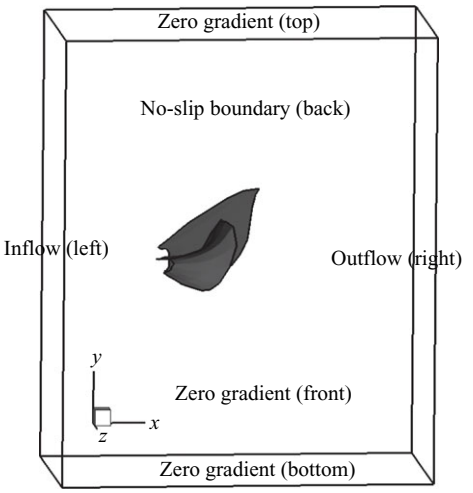


FIGURE 4. Schematic of the computational domain employed in the current simulations, which includes the velocity boundary conditions employed on the various boundaries. The figure shows the conformation of the fin at two time instants.

which is the longest ray of the bluegill pectoral fin, is used as the primary length scale for the current flow and denoted as $L_{fin}$. The fin stroke frequency $f$ is used as the time scale, and the mean fish velocity $U_\infty$ is chosen as the velocity scale. The key non-dimensional parameters for the fin are the Reynolds number ($Re$) defined as $L_{fin}U_\infty/\nu$ and the Strouhal number ($St$) defined as $fL_{fin}/U_\infty$. The amplitude of the stroke can be encapsulated in the stroke amplitude parameter defined as $A_s = D_{tip}/L_{fin}$, where $D_{tip}$ is the maximum linear distance travelled by the tip of the fourth fin ray.

The fish studied here ranged in size from about 14.5 cm to 17.5 cm, with fin sizes ranging from 3.5 cm to 4 cm. The nominal conditions for the current simulations correspond to a fish with a fin size $L_{fin}$ of 4 cm travelling nominally at a speed of about 1.1 body lengths per second (BL $s^{-1}$, which corresponds to 0.16 m $s^{-1}$ for this particular fish) and flapping its fin at 2.17 Hz. This results in a fin Reynolds number of about 6300 and a fin Strouhal number of 0.54. Furthermore, the tip amplitude $D_{tip}$ is about 3.4 cm, which leads to a normalized fin amplitude $A$ of 0.85.

Figure 4 shows the nominal computational domain used in the current study. The domain size normalized by $L_{fin}$ is $3.8 \times 4.5 \times 1.8$. The fin is placed along one of the boundaries of the domain, and a no-slip, no-penetration boundary condition is applied on this wall to mimic the effect of the fish body. Since the fin is held out from the body during most of the thrust-producing periods of the stroke, the attached boundary layer that develops on the body of the fish during forward travel is expected to have a minimal effect on the flow around the fin. The boundary conditions used on the other boundaries are as follows: at the left inflow boundary, we specify the flow velocity to be equal to $(U_\infty, 0, 0)$, whereas on the right outflow boundary, we apply a convective boundary conditions that allows the vortex structures to exit the boundary without any spurious reflections (Dong *et al.* 2006). On all the lateral boundaries, we apply a far-field boundary condition which amounts to specifying the streamwise velocity component to $U_\infty$ and setting the normal gradients of the other velocity components to zero. We have employed a large, $201 \times 193 \times 129$ (4.9 million points) non-uniform Cartesian grid (shown in figure 5) for the $Re = 6300$ simulations. A rectangular region around the fin and the wake is provided the highest resolution

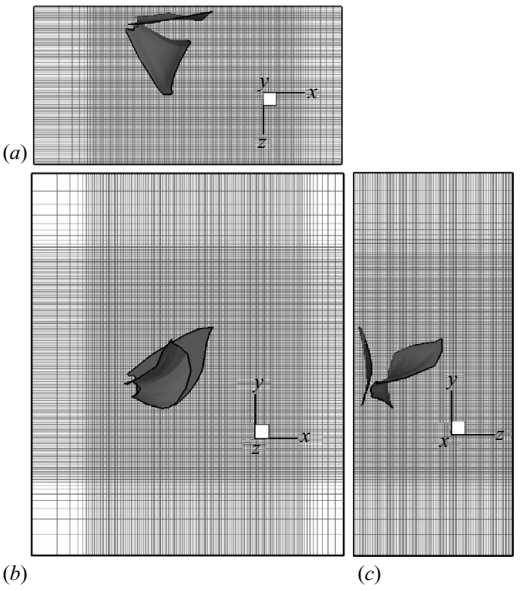


FIGURE 5. The grid employed in the current study: (*a*) top view; (*b*) side view; (*c*) front view. The figure shows the conformation of the fin at two time instants.

with an isotropic grid spacing of $0.012L_{fin}$, and this region has a $153 \times 159 \times 113$ (2.75 million points) grid. Beyond this region of high resolution, the grid is stretched out towards the outer domain boundaries. The above domain and grid specifications are chosen based on previous fin simulations at a lower Reynolds number ($Re_f = 1140$; Bozkurttas *et al.* 2006; Mittal *et al.* 2006), and the adequacy of these choices has been examined by grid and domain dependency studies. For lower-Reynolds-number simulations described in the current study, we use a smaller grid which is described in Mittal *et al.* (2006, 2008). A more detailed discussion of the grid and domain dependency study is available in Bozkurttas (2007).

## 4. POD analysis of pectoral fin kinematics

POD (also known as PCA in some fields of application) is a powerful method for data analysis aimed at obtaining low-dimensional approximate descriptions of a high-dimensional process or dataset (Liang *et al.* 2002). The most remarkable feature of the POD is its optimality: it provides the most efficient way of capturing the dominant components of any dataset with only a finite and often surprisingly few number of modes. In gait analysis, PCA has yielded insights into human walking strategies and the interrelationships in terms of temporal, kinematic and kinetic variables. Urtasun *et al.* (2004) have used PCA to identify invariant or common features within the whole body kinematics of a contemporary dance movement pattern. Representing motions as linear sums of principal components has become a widely accepted animation technique (Alexa & Mueller 2000; Troje 2000).

POD of a given dataset can be obtained either through eigenvalue decomposition of the data covariance matrix or through singular value decomposition (SVD) of the data matrix. In the current study we have employed the SVD method, and close connections and equivalence of these various methods can be found elsewhere (Liang

*et al.* 2002). Since the theory of POD is well established, we will only describe here the SVD procedure as applied to the current fin kinematic dataset.

### 4.1. *SVD of the pectoral fin kinematics*

SVD can be considered an extension of eigenvalue decomposition for non-square matrices. The starting point for the SVD analysis in the current case is the dataset that contains the displacement in space of the 280 nodes on the surface of the fin at 19 distinct instants in time. Note that the motion of the fin is assumed to be periodic in time, and therefore, the 20th time instant is the same as the 1st time instant. This matrix (denoted by $\Delta \boldsymbol{X}$) is as follows:

$$\Delta \boldsymbol{X} = \begin{bmatrix} \Delta x_1(t_1) & \Delta y_1(t_1) & \Delta z_1(t_1) & \dots & \dots & \Delta x_{280}(t_1) & \Delta y_{280}(t_1) & \Delta z_{280}(t_1) \\ \Delta x_1(t_2) & \Delta y_1(t_2) & \Delta z_1(t_2) & \dots & \dots & \Delta x_{280}(t_2) & \Delta y_{280}(t_2) & \Delta z_{280}(t_2) \\ \vdots & \vdots & \vdots & \vdots & \vdots & \vdots & \vdots & \vdots \\ \vdots & \vdots & \vdots & \vdots & \vdots & \vdots & \vdots & \vdots \\ \Delta x_1(t_{19}) & \Delta y_1(t_{19}) & \Delta z_1(t_{19}) & \dots & \dots & \Delta x_{280}(t_{19}) & \Delta y_{280}(t_{19}) & \Delta z_{280}(t_{19}) \end{bmatrix}_{19\times 840} \tag{4.1}$$

An SVD of the above displacement matrix can be written as

$$\Delta \boldsymbol{X}_{n\times m} = \boldsymbol{U}_{n\times n} \Sigma_{n\times m} \boldsymbol{V}^T_{m\times m}, \tag{4.2}$$

where $\boldsymbol{U}_{n\times n}$ and $\boldsymbol{V}^T_{m\times m}$ are two orthogonal unitary matrices; $n$ is the number of datasets (which in this case is the number of time steps) and $m$ is the number of data points in each set (which is equal to the number of surface nodes on the fin); $\Sigma_{n\times m}$ is a diagonal matrix in which the diagonal values are called the singular values of $\Delta \boldsymbol{X}$ (and also $\Delta \boldsymbol{X}^T$), which are unique. The diagonal elements $\Sigma_{ii}$ consist of $r = \min(n, m)$ non-negative numbers $\sigma_i$, which are arranged in descending order, i.e. $\sigma_1 \geqslant \sigma_2 \geqslant \cdots \geqslant \sigma_r \geqslant 0$. Within the SVD procedure, the $\sigma_i$ values are the square roots of the eigenvalues of $\Delta \boldsymbol{X} \Delta \boldsymbol{X}^T$ (and $\Delta \boldsymbol{X}^T \Delta \boldsymbol{X}$), whereas the eigenvectors of $\Delta \boldsymbol{X} \Delta \boldsymbol{X}^T$ and $\Delta \boldsymbol{X}^T \Delta \boldsymbol{X}$ make up the columns of $\boldsymbol{U}$ and $\boldsymbol{V}^T$ respectively. In the above expression, $\boldsymbol{U}$ represents the change of each mode with time, and $\boldsymbol{V}$ contains the eigenvectors corresponding to the spatial distribution of the modes.

The singular values $\sigma_i$ can be interpreted as the weight contributions of each mode in the POD decomposition. Thus, the 'shape' of any particular mode (say the $k$th mode) can be extracted by zeroing out all the singular values except for the $k$th value, and reconstructing from the SVD as in (4.2). Similarly, lower-dimensional (say rank $K < r$) approximations to the dataset can be obtained by using an approximation to $\Sigma$ denoted by $\Sigma_K$ wherein $\sigma_{K+1} = \sigma_{K+2} = \cdots = \sigma_r = 0$ and reconstructing from the SVD as follows:

$$\Delta \boldsymbol{X}_K = \boldsymbol{U} \Sigma_K \boldsymbol{V}^T. \tag{4.3}$$

The displacement matrix $\Delta \boldsymbol{X}$ is now subjected to SVD. In the current study, we employ a MATLAB program to compute the SVD. As expected, the SVD leads to 19 distinct singular values, and the singular value spectrum of the fin kinematics is shown in figure 6 along with a cumulative plot for the same data. The singular values are normalized by the sum of all singular values, and therefore, the cumulative values sum to unity. A number of interesting observations can be made from this plot. First, the singular value spectrum shows three distinct ranges: the first between Modes 1–5 in which we see a rapid decrease in the amplitude, the second from Modes 5–11 in

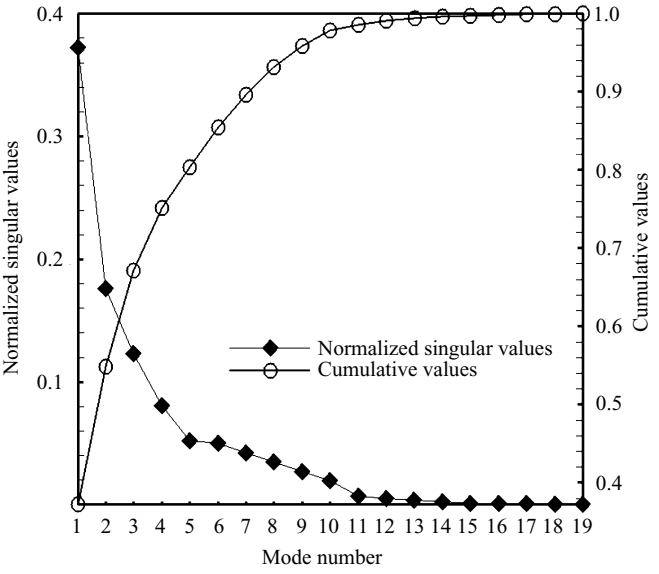


FIGURE 6. The POD spectrum for the pectoral fin kinematics. The left ordinate shows $|\sigma_i|/\sum|\sigma_i|$, and the right ordinate shows the cumulative value of the left ordinate.

which there is a much slower reduction in amplitude and, finally, the range from Modes 12–19 that has negligible (<2 %) total contribution. The rapid initial decrease in the spectrum is significant in that it suggests that a small number of modes contain most of the essential features of the fin gait. In fact, the cumulative values show that the first two, three and five modes capture about 55 %, 67 % and 80 % respectively of the total motion. In fact, only the first mode captures close to 37 % of the motion of the fin, which is a clear demonstration of the ability of POD to represent the dataset with the least possible number of modes.

The gait corresponding to individual modes can be extracted as described above, and the surface conformations for each of these extracted modes are then constructed using the original fin mesh with triangular elements. The first three modes are highly distinct and relatively easy to interpret, and we briefly describe the key qualitative features of these modes. Figure 7 shows Modes 1–3 at seven different times during one fin-beat cycle. Also shown on the left for direct comparison are the fin kinematics from the experiment (also called the 'Mode-All' case, since it contains all the POD modes). In these figures, the shades reflect the distance from the body in mm. Mode 1 involves considerable movement away from the body in what we call the 'cupping' motion in which the fin cups forward as it is abducted. It leads to a rapid acceleration of the fin dorsal and ventral edges, forming two leading edges from them. This mode is actively produced by the fish through differential angular displacement of the fin rays.

Mode 2 is named an 'expansion' mode in which the fin expands to present a larger surface area during adduction. The increase in fin surface area during the adduction phase can be observed in figure 7(*b*). This mode also includes a slight movement away from the body at the middle region of the fin around distal edge during the adduction phase. This expansion mode is also a result of active angular motion of the fin rays by the fish.

Mode 3 is a wave-like motion in the spanwise direction, which occurs along the dorsal edge of the fin. It presents as a rapid spanwise 'flick' of the dorsal edge of the

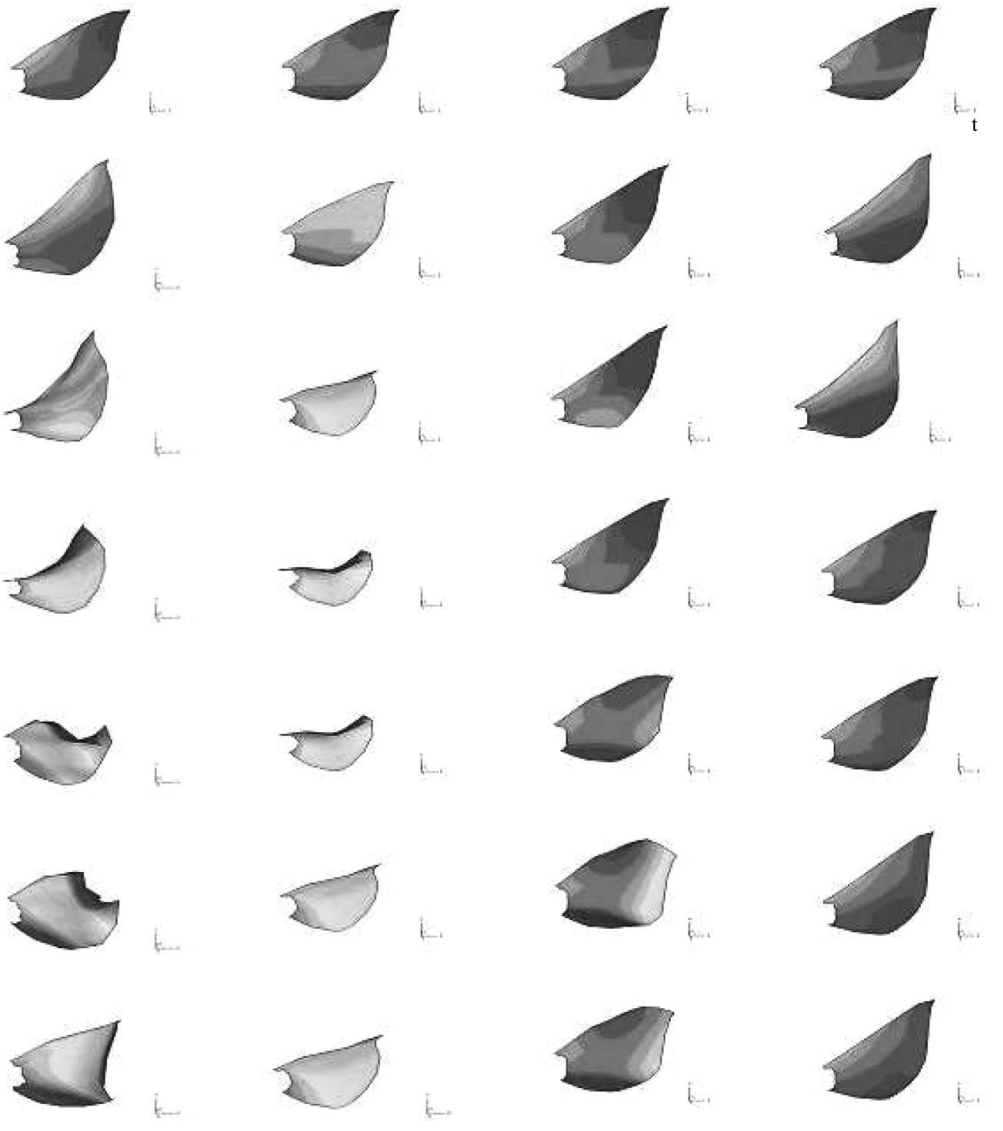


(*a*) Mode-All (*b*) Mode 1 (*c*) Mode 2 (*d*) Mode 3

FIGURE 7. Experimental kinematics (also called the Mode-All case) and the first three POD modes of the fin kinematics during the fin-beat cycle in steady forward swimming.

fin tip during the abduction phase. The spanwise curvature associated with this mode is most easily viewed in the third plot corresponding to this mode, where the dorsal edge is found to curve upwards. In contrast to Modes 1 and 2, this mode is primarily a result of flow-induced deformation. This can be deduced from the fact that there are no muscles in the fin rays or in the fin that could produce spanwise deformation in the fin. Furthermore, the spanwise deformation is in the direction of the flow relative to the fin motion, which supports the assertion that this mode is flow-induced. The rest of the modes in the spectrum are associated with relatively small motions that are not very distinct. We therefore do not describe these individually, although we

will consider the effect of higher modes on the kinematics and hydrodynamics in the following sections.

It should be pointed out that deeper insights into the fin kinematics could be gained by constructing a structural model of the fin and subjecting this model to an eigenelastic and/or fluid-structure interaction (FSI) study. Comparison of the eigenelastic modes with the POD modes could help, for example, to delineate passive deformation modes from active deformation modes However, such an analysis requires parameterization of the structural properties of the fin, as well as the compliance and motor forces/torques at roots of the fin rays. Unfortunately, experiments that would produce such parameterizations are extremely difficult to conduct, and no such parameterization is currently available.

### 4.2. *Low-dimensional models of the fin gait*

POD has decomposed the fin kinematics into its orthogonal components and helped us understand the key features of bluegill's pectoral fin movement in steady forward swimming. The POD results can also be used to reconstruct low-dimensional approximations of the Mode-All case using a subset of the orthogonal modes. Lower-dimensional models of the fin gait are synthesized by successively adding modes to Mode 1. Figure 8 shows the surface snapshots at eight different times during one fin-beat cycle for Mode 1, Mode 1+2 and Mode 1+2+3 in comparison to the complete (Mode-All) motion. In these figures the contours are the same as figure 7. Similarity between the fin shapes for Mode 1+2+3 and the Mode-All/experiment cases is evident in this figure. Removal of higher POD modes from the kinematics is analogous to filtering the experimental data in space and time.

The POD analysis suggests one natural approach to the development of the robotic fin. Since a small number of modes capture a significant portion of the motion, it stands to reason that a systematic procedure to developing a robotic fin would to be to design actuation mechanisms that reproduce a small number of these modes. The question that remains to be answered is what kind of propulsive performance can we expect from these lower-dimensional fin models, and how does the performance scale as we include additional modes? This will allow us to make a rational compromise between complexity of fin design and fin performance. It should be noted here that the propulsive performance is a consequence of the flow associated with these lower-dimensional fin models. Thus, even though the modes are kinematically linear (and therefore additive), the propulsive performance is not expected to scale linearly with the modes, since the flow is governed by the Navier–Stokes equations which are nonlinear. Thus, the answer to the above question requires that we explicitly determine the propulsive performance for these lower-dimensional fin models. The following section describes our approach to answering this question.

## 5. Hydrodynamics of low-dimensional fin gaits

Simulations have been carried out using the precise fin kinematics extracted from the experiments (this case is termed here as Mode-All), and these have been discussed in some detail in Lauder & Madden (2006) and Mittal *et al.* (2006). As pointed out before, the nominal conditions for the current simulations correspond to a fin Reynolds number of about 6300 and a fin Strouhal number of 0.54, and these match the experimental conditions of Lauder & Madden (2006). Results from these simulations and both qualitative and quantitative comparisons with the companion experiments are presented in Dong *et al.* (2009). Although the main focus of the

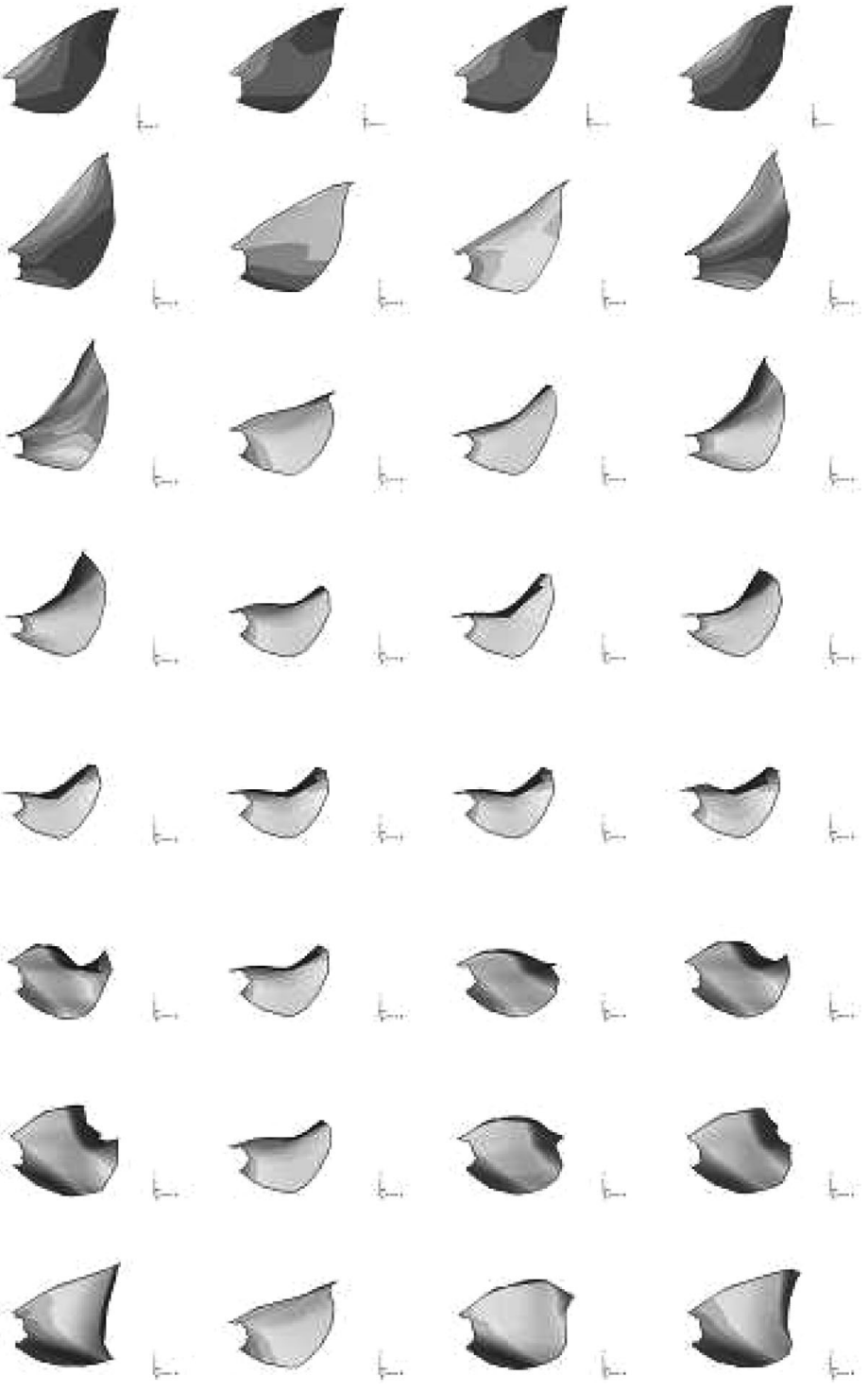

(*a*) Mode-All (*b*) Mode 1 (*c*) Mode 1+2 (*d*) Mode 1+2+3

FIGURE 8. Surface conformations over one cycle of first three low-dimensional gaits synthesized from the POD modes with comparison to the Mode-All case.

| Gait | *Re* | *St* |
|---|---|---|
| Mode-All (experimental kinematics) | 6300 | 0.54 |
| POD Mode 1 | 6300 | 0.54 |
| POD Mode 1+2 | 6300 | 0.54 |
| POD Mode 1+2+3 | 6300 | 0.54 |
| POD Mode 1+2+3+4+5 | 6300 | 0.54 |
| POD Mode 1+2+3 | 1440 | 0.54 |
| POD Mode 1+2+3 | 540 | 0.54 |
| POD Mode 1+2+3 | 1440 | 0.41, 0.7 |
| POD Mode 1+2+3 | 0 | $\infty$ |

TABLE 1. Summary of cases discussed in current study.

current work is the analysis of the hydrodynamics and propulsive performance of low-dimensional models based on POD modes, some key results for the Mode-All case are also included here, since comparison against this case is key to understanding the scaling of the thrust performance as the dimensionality of the models is increased. All the results presented here have been obtained by simulating the flow over six fin strokes. In computing mean quantities, we have discarded the first two strokes, and all plots of instantaneous quantities correspond to the third cycle in the stroke by which time the flow has reached a well-established stationary state.

In the current study we focus on the following lower-dimensional gaits: Mode 1, Mode 1+2, Mode 1+2+3 and Mode 1+2+3+4+5. In the first part of this paper, all these gaits are studied at a Reynolds number of 6300 and Strouhal number of 0.54. Thus, dynamical similarity between the Mode-All case and the low-dimensional models is maintained, and this allows us to isolate the effect of model dimensionality on the fin propulsive performance.

Subsequent to this, we assess the scaling of the propulsive performance of the fin wherein two sets of simulations have been carried out for the Mode 1+2+3 gait. As will become clear subsequently, this particular gait represents the simplest gait that captures the key hydrodynamic features of the fish fin. As such, we consider this gait to be a good candidate for a robotic pectoral fin design and investigate scaling issues for this gait. Reynolds number scaling of this gait has been examined by simulating flow at the experimental Strouhal number of 0.54 with two additional Reynolds number (540, 1440). On the other hand, in order to examine the Strouhal number scaling, we fix the Reynolds number at 1440 and examine the propulsive performance at two additional Strouhal numbers ($St = 0.41, 0.7$). Finally, we also examine the use of the fin in a 'starting' manoeuvre, which corresponds to $St = \infty$. Table 1 summarizes the simulation parameters of the POD-synthesized fin gaits presented in this study.

### 5.1. *Effect of model dimensionality on fin hydrodynamics and performance*

In this section, we describe the effect of increasing the dimensionality of the fin motion on the propulsive performance. We first focus on the qualitative features of the flow for these low-dimensional gaits and subsequently address the effect of model dimensionality on the quantitative characteristics of the fin, including force production and propulsive efficiency.

Figure 9 shows the vortex structures at two time instants in the stroke for the Mode-All case. The vortex structures are identified by plotting contours of the 'swirl strength' which is the magnitude of the imaginary part of the complex eigenvalue of the velocity deformation tensor (Soria & Cantwell 1993; Mittal *et al.* 2006). In

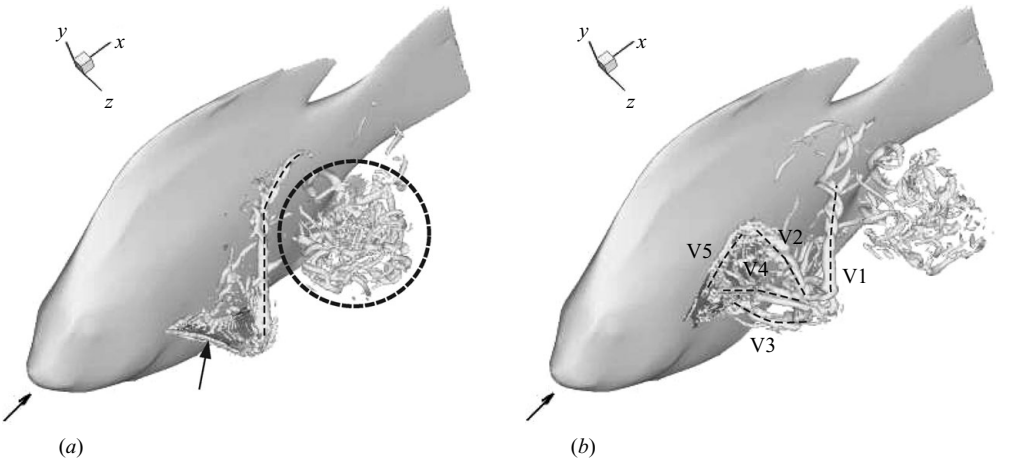


FIGURE 9. Wake structures for the Mode-All case (i.e. kinematics directly from the experiment) at $Re = 6300$ and $St = 0.54$: (*a*) $t/\tau = 2/3$; (*b*) $t/\tau = 1.0$. The fish body is only shown for context and not included in simulations.

these figures, the body of the fish is shown for visualization purposes only and is not included in the simulations. Figure 9(*a*) shows the vortex structures at $t/\tau = 2/3$, which is immediately after the fin has initiated the adduction phase. One of the most visible vortex structure at this phase is the strong tip vortex (identified with a dashed line) that extends from the tip of the fin all the way into the wake over a distance that is roughly twice the size of the fin. Also visible is the dorsal-edge vortex on the anterior surface of the fin (highlighted by an arrow) that is formed due to the rapid forward motion of the fin during adduction. The vortex conglomeration associated with the previous fin stroke (identified by a dashed circle) has convected further downstream by this time.

Figure 9(*b*) shows the vortex structures at $t/\tau = 1$, which represents the completion of the fin stroke, and a number of distinct vortex structures are observed at this phase of the cycle. The spanwise tip vortex formed during the abduction phase (denoted as V1 in the figure) is now completely separated from the fin and extends far into the wake. Also visible is another tip vortex (identified as V2), which is formed at the spanwise tip of the the fin due to fin adduction. There are also two vortices (V3 and V4) which can be identified, and these are vortices shed by the ventral and dorsal edges respectively. Finally, at this phase, we also identify an attached dorsal-edge vortex (V5), which is formed after the vortex (V4) formed earlier in the adduction phase has shed from the dorsal edge. Thus, at the end of the stroke, there are a number of distinct vortex structures that are created and released by the fin. These vortex structures are subject to mutual induction effects as they convect downstream, which leads to deformation (stretching and turning) of the vortex filaments and the eventual development of a highly complex conglomeration of vortices further downstream in the wake.

Similar views of the vortex structures are given in figures 10–13, for the Mode 1, Mode 1+2, Mode 1+2+3 and Mode 1+2+3+4+5 gaits respectively. It can be observed that the vortex topology of the Mode 1 gait is quite different from that of the Mode-All case. In particular, the strong abduction tip vortex (V1) is virtually absent, and the other vortex structures (adduction tip vortex and dorsal and ventral edge vortices) are also not identifiable. The Mode 1+2 gait on the other hand,

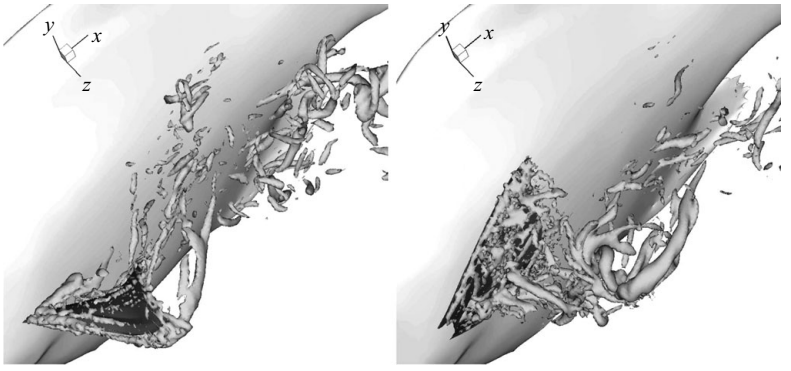


(*a*) (*b*)

FIGURE 10. Wake structures for the POD Mode 1 gait at $Re = 6300$ and $St = 0.54$.

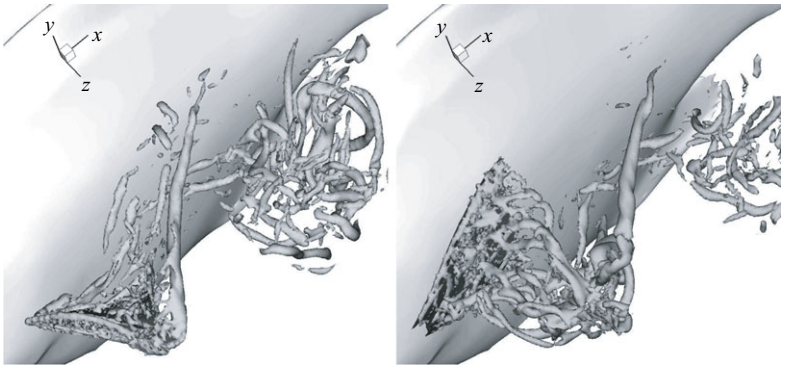


(*a*) (*b*)

FIGURE 11. Wake structures for the POD Mode 1+2 gait at $Re = 6300$ and $St = 0.54$.

exhibits a clearly identifiable abduction tip vortex, although this vortex is not as well-developed as the Mode-All case. The Mode 1+2 approximation also shows an attached dorsal-edge vortex during the abduction phase. Furthermore, during the adduction phase, the Mode 1+2 approximation produces weak dorsal- and ventral-edge detached vortices as well as an adduction tip vortex, although all of these vortices are not as well-formed as for the Mode-All case.

The Mode $1 + 2 + 3$ gait exhibits a wake (shown in figure 12) that is quite similar to the Mode-All case. A strong abduction tip vortex is followed by clearly identifiable dorsal- and ventral-edge detached vortices during the adduction phase as well as a tip vortex during this phase of the motion. Thus, the results seem to indicate that three POD modes suffice to reproduce most of the key features of the wake topology of the fin. Finally, the Mode $1 + 2 + 3 + 4 + 5$ wake shown in figure 13 is virtually identical to the Mode-All wake.

The time variations of thrust, lift and spanwise force coefficients are presented for all the low-dimensional gaits and compared to the Mode-All case in figure 14(*a–c*) respectively. The force coefficient for a generic force $F$ is defined as

$$C_F = \frac{F}{1/2\rho U_\infty^2 A_{fin}}, \tag{5.1}$$

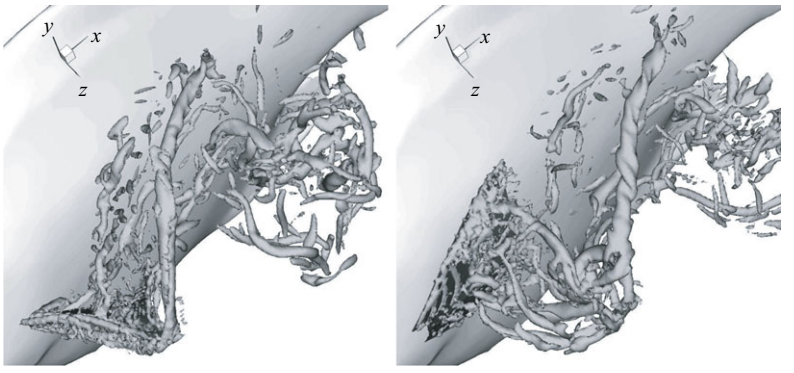


(*a*) (*b*)

FIGURE 12. Wake structures for the Mode $1 + 2 + 3$ gait at $Re = 6300$ and $St = 0.54$.

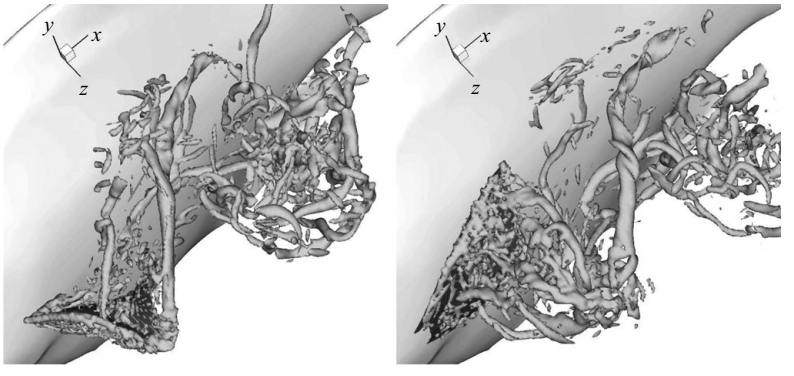


(*a*) (*b*)

FIGURE 13. Wake structures for Mode $1 + 2 + 3 + 4 + 5$ gait at $Re = 6300$ and $St = 0.54$.

where $A_{fin}$ is the nominal fin area; $\rho$ is the density of the fluid; and $U_\infty$ is the free stream velocity. The force components are calculated by directly integrating the computed pressure and shear stress on the fin surface. For instance, if $\sigma$ is the traction over the fin surface, then the thrust is given by

$$T(t) = \int_{A_{fin}} \sigma_1 \mathrm{d}A\,, \tag{5.2}$$

where $\sigma_1$ is the component of the surface traction in the direction of thrust.

Another key parameter associated with the hydrodynamic performance of the fin is the propulsive efficiency. In the current context, propulsive efficiency is defined as

$$\eta = \frac{\bar{P}_{out}}{\bar{P}_{in}}, \tag{5.3}$$

where $\bar{P}_{out}$ is the mean useful power produced by the fin over one stroke and $\bar{P}_{in}$ is the mean total power input to the fin over the stroke. The mean useful power is equal to $\bar{T}U_\infty$, where $\bar{T}$ is the mean thrust produced by the fin and $U_\infty$ is mean forward velocity of the fish. The total mean mechanical input power to the fin can then be

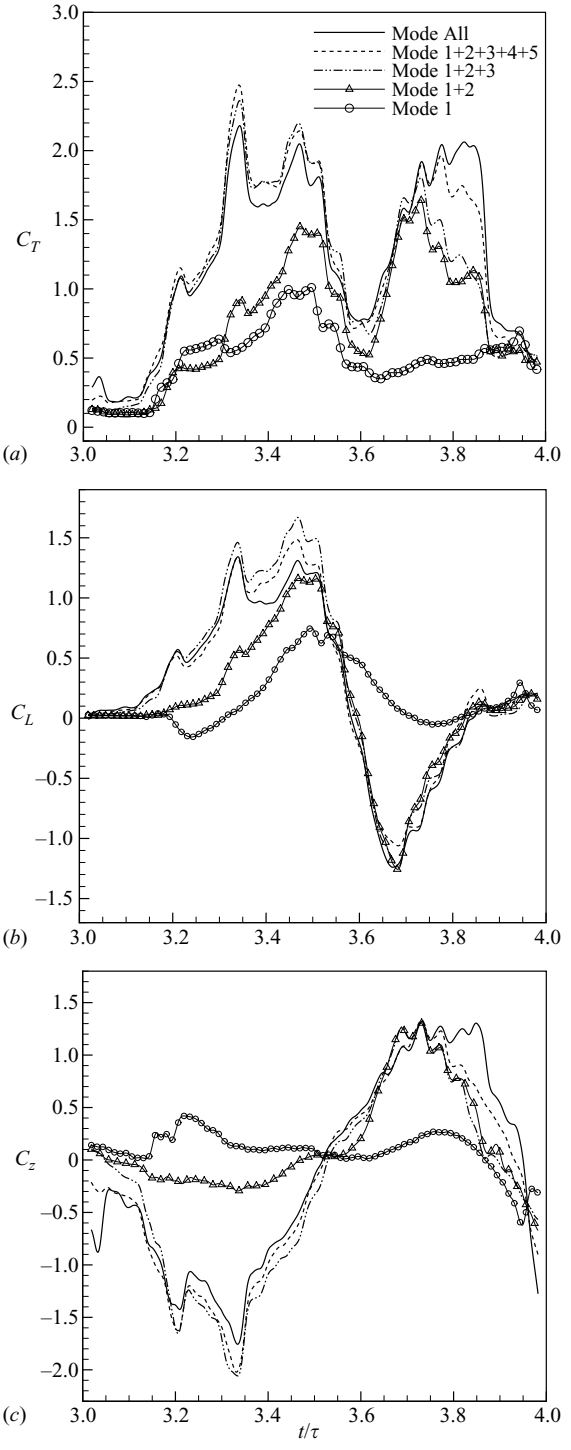


FIGURE 14. Comparison of the time variation of force coefficients between the Mode-All and POD-synthesized gaits at $Re = 6300$ and $St = 0.54$: (*a*) thrust; (*b*) lift (or vertical force); (*c*) spanwise force. The abduction phase extends from $t/\tau = 0$ to $t/\tau = 0.57$, and the remaining portion of the stroke is the adduction phase.

computed as

$$\bar{P}_{in} = \frac{1}{M\tau} \int_{M\tau} \int_{A_{fin}} (\sigma \cdot \boldsymbol{V}) \, \mathrm{d}A \, \mathrm{d}t, \tag{5.4}$$

where $\boldsymbol{V}$ is the local velocity of the fin surface. A detailed discussion regarding the efficiency is presented in Dong *et al.* (2009). Efficiency values for the low-dimensional models of the fin gait are also given in table 2.

Several observations on how each POD mode contributes to the performance of the fin can be made from these results. It should be noted that only Mode 1 can be simulated by itself. However, given the underlying nonlinearity of the flow, the contribution of Modes 2 and 3 are investigated by considering the differences in the performance from the lower-level gait. Thus, the effect of Mode 2 on performance is obtained by analysing the difference between the performance of the Mode 1 and Mode 1+2 cases. Similarly, the effect of Mode 3 on fin performance can be assessed by comparing the performance of the Mode 1+2+3 case with that of the Mode 1+2 case.

First of all, figure 14(*a*) shows that all POD-synthesized gaits produce thrust through the entire fin-beat cycle as in the Mode-All case. This can be seen as a distinguishing characteristic of the fish fin function, since it is known that rigid oscillating wings produce drag in some phase of their thrust-producing motion Dong *et al.* (2006). In Dong *et al.* (2009) we have also performed a detailed comparison of the peak-to-peak values of all the force coefficients with the companion experiments of **?**, and the comparison is found to be quite reasonable. In these experiments the acceleration of the centre of mass of the fish body was tracked using high-speed videogrammetry, and this was used to determine the acceleration of the fish during steady state swimming. In addition, Drucker & Lauder (2000) have measured the drag on the body of a sunfish, and using this estimate and assuming that for steady swimming both the fins together produce a force that counteracts this body drag, we get an estimate a fin thrust coefficient of $1.03 \pm 0.23$. This value is a reasonable match to the computed fin thrust coefficient of 1.18.

The second key observation is that all POD-synthesized gaits except for Mode 1 show two main peaks of thrust, one in the abduction phase and one in the adduction phase. Two peaks of thrust have been confirmed by the experiments of the bluegill's pectoral fin in steady forward motion as well (**?**). Mode 1 captures the first peak of the thrust in the abduction phase with a smaller amplitude, but the second peak is almost non-existent. As a reminder, Mode 1 is the so-called cupping movement of the fin, and it represents 37 % of fin motion based on the normalized singular values given in POD spectrum (see figure 6). The time-averaged thrust coefficient for the Mode 1 case is calculated as $\overline{C_T} = 0.5$, which corresponds to 42 % of the mean thrust produced by the Mode-All case.

Focusing now on the Mode 1+2 gait, we find that the addition of Mode 2 generates slightly higher thrust during the abduction phase in comparison to Mode 1. However, the major impact of the addition of Mode 2 is on the thrust during the adduction phase. With this mode added, a second peak during adduction appears, albeit with a smaller amplitude than the Mode-All case. An examination of the kinematics of Mode 1 and Mode 2 suggests that the key feature that Mode 2 adds is the expansion (area increase) of the fin perpendicular to the flow direction during the adduction phase. Thus, Mode 2 essentially introduces kinematics analogous to the power phase of a 'paddling' stroke wherein, on the backstroke, the paddle surface is made perpendicular to the direction of the motion of the paddle. The impact of this

| | Motion (%) | $\overline{C_T}$ | $\overline{C_L}$ | $\overline{C_Z}$ | $\eta$ | Thrust production (%) |
|---|---|---|---|---|---|---|
| Mode-All | 100 | 1.18 | 0.22 | −0.16 | 0.60 | 100 |
| POD Mode 1 | 37 | 0.50 | 0.16 | 0.087 | 0.73 | 42 |
| POD Mode 1+2 | 45 | 0.75 | 0.11 | 0.13 | 0.59 | 64 |
| POD Mode 1+2+3 | 67 | 1.09 | 0.29 | −0.26 | 0.53 | 92 |
| POD Mode 1+2+3+4+5 | 80 | 1.18 | 0.22 | −0.16 | 0.60 | 100 |

TABLE 2. Comparison of the hydrodynamic performance for the Mode-All and POD-synthesized gaits at $Re = 6300$ and $St = 0.54$.

on the force production is quite significant; the time-averaged thrust value for Mode 1+2 is computed as $\overline{C_T} = 0.75$ (see table 2), and this is about 64 % of the thrust of the Mode-All case. It should also be pointed out that Mode 1+2 constitutes about 55 % of the complete fin motion but captures 64 % of the thrust of the Mode-All case.

The addition of Mode 3 is examined by simulating the Mode 1+2+3 gait and comparing with the lower-dimensional gaits. As shown in figure 14(*a*), the inclusion of Mode 3 improves the thrust performance considerably in both abduction and adduction phases. In fact, the Mode 1+2+3 gait captures the thrust production of Mode-All case quite well for the first three quarters of the cycle. The superior performance of this gait is an indication of the significance of spanwise tip flick represented by Mode 3. The mean thrust is $\overline{C_T} = 1.09$ for this case, and this is only 8 % lower than that of the Mode-All case. Clearly, the missing part is due to the remaining modes in the POD spectrum. Thus, Mode 1+2+3 which constitutes 67 % of the motion captures 92 % of the complete thrust. It should be reiterated that unlike Modes 1 and 2 which are produced due to active deformation through angular motion of the fin rays, Mode 3 is primarily due to flow-induced deformation. Thus, Mode 3 can be considered to be a result of the fin motion (as defined by the addition of Modes 1 and 2) and the spanwise flexibility of the fin.

The Mode 1+2+3+4+5 gait has been studied as the highest level of approximation, and it constitutes about 80 % of the fish fin motion. The addition of Mode 4 and Mode 5 enhances the thrust production over the Mode 1+2+3 gait during the adduction phase. However, there is still a slight discrepancy with the Mode-All case at the end of the cycle. This is compensated by better performance during the abduction phase, and hence, the Mode 1+2+3+4+5 gait recovers a mean thrust which is nearly the same as that of the Mode-All case. Since Mode 4 and Mode 5 movements are not as distinct as the lower modes (Mode 1–3) and since the Mode 1+2+3 gait itself produces 92 % of the thrust produced by the Mode-All case, the Mode 1+2+3 gait emerges as one that might be appropriate for biorobotic fin design. The above also suggests the effectiveness of the POD method for decomposing the fin kinematics into its minimal essential components and, in particular, to set a lower bound for the kinematics that are acceptable in well-performing bio-inspired pectoral fin. It should be noted that these higher modes also have a relatively more complex spatial and temporal structure, and replication of these modes in a robotic pectoral fin would likely require a larger number of actuators and a higher degree of control. The POD analysis, coupled with computational modelling, conclusively shows that replication of these modes is not required, and this can substantially ease the design challenge for such propulsors.

It should be pointed out that both the Mode 1+2+3 and the Mode 1+2+3+4+5 approximations predict a higher thrust than the Mode-All case during abduction, whereas both produce lower thrust during adduction. Thus, addition of the modes does not produce a monotonic approach to the Mode-All case. This is, however, not unexpected due to the underlying nonlinearity of the flow.

The lift curve trends are similar for all gaits except for Mode 1 (see figure 14*b*). All POD-synthesized gaits and the Mode-All case have a positive peak in abduction phase and a negative peak in the adduction phase. It should be noted that the peak-to-peak values of lift are lower than that of thrust, which is one key for the superior efficiency compared to the rigid flapping fins. The time-averaged values of the lift coefficient presented in table 2 are small for all cases. The advantage of small mean vertical force is abundantly clear; it reduces the vertical drift in the trajectory of the fish as it swims forward. What is interesting is that the fish manages to effectively cancel out the positive lift in the abduction phase with a nearly equal negative lift in the adduction phase despite very different kinematics in these two phases.

Figure 14(*c*) shows the time variation of the spanwise force coefficients, and these behave similarly for Mode 1+2+3, Mode 1+2+3+4+5 and the Mode-All case. They all have a negative peak during the abduction phase and a positive one during adduction. Although Mode 1 and Mode 1+2 have a different trend in time variations of this force component, the mean values calculated for all POD gaits are small in comparison to thrust. The same explanation holds for the spanwise force; the fish needs to keep side forces as small as possible for stability and station-keeping purposes. It should be noted that similar behaviours in the lateral forces would be desirable in the design of biorobotic fin kinematics.

Values of propulsive efficiency are calculated using (5.3) and are also included in table 2. Mode-All and Mode 1+2+3+4+5 have the same efficiency values of 60 %, and Mode 1 is the most efficient gait with a 73 % efficiency. Mode 1+2+3 gait has an efficiency of 53 % which, although the lowest, is only about 12 % lower than the Mode-All case. The Mode 1+2 gait has an efficiency of 59 %, which is nearly the same as the Mode-All case. It is interesting to note that the propulsive efficiency has a highly non-monotonic variation as the model dimensionality is increased, and this is, yet again, a clear manifestation of the underlying nonlinearity of the fluid flow.

## 6. Reynolds-number-scaling effects

Two non-dimensional parameters that can potentially affect the performance of the fin are the Reynolds number ($Re = U_\infty L_s/\nu$) and Strouhal number ($St = L_s f/U_\infty$). Examination of the scaling of the fin performance with these two parameters allows us to gain a better insight into the fundamental mechanisms of force generation. Biologically inspired, flapping-fin-propelled autonomous underwater vehicles of sizes ranging from a few inches to a metre or more in length are being developed by various groups. Thus, a Reynolds number scaling also allows us to address the practical question of how the performance of the fin is expected to change with changes in size, speed and frequency. and given that Mode 1+2+3 despite employing only three modes recovers much of the propulsive performance of the Mode-All case, it is an excellent basis for a design of a biorobotic pectoral fin. In fact, preliminary fin designs by Tangorra *et al.* (2007) have attempted to mimic these three modes. Given this, we have examined the issue of Reynolds and Strouhal number scaling for the Mode 1+2+3 case.

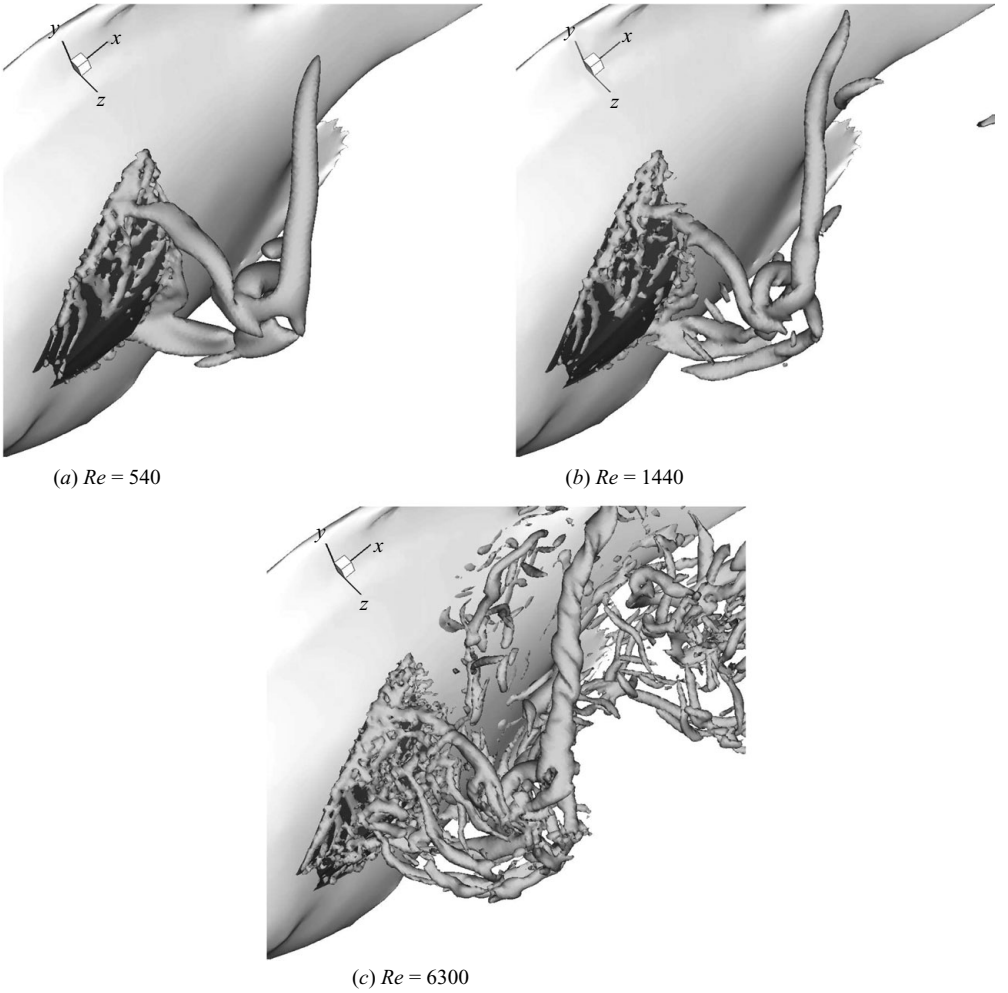


(*a*) $Re = 540$ (*b*) $Re = 1440$

(*c*) $Re = 6300$

FIGURE 15. Wake structures for the Mode $1 + 2 + 3$ gait at $St = 0.54$ and $t/\tau = 1.0$.

In the first set of simulations, we examine the scaling of the fin performance with Reynolds number by simulating the fin flow for two additional values of 540 and 1140. Given the nominal Reynolds number of 6300, the above simulations represent a range spanning an order of magnitude in this parameter. In these simulations, $St$ is kept constant at the nominal value of 0.54. A practical way to interpret this set of simulations is as follows: if we were to scale the size of the fish (or of a biorobotic underwater vehicle employing such fins) by a factor of $\lambda$, then the Reynolds number would scale by a factor of $\lambda^2$, since the fin size and velocity would each change by a factor or $\lambda$. Note that here we assume that the fish/vehicles of different size continue to swim at the same speed in terms of BL $s^{-1}$. At the same time, since both the fin size and the forward velocity change by the same factor, the Strouhal number remains the same. Thus, reduction of the Reynolds number to 1140 and 540 can be interpreted as reduction to 43 % and 29 % of the nominal size respectively.

The wake vortex structures for the three cases are compared in figure 15, and it is observed that although the structures get simpler with decreasing Reynolds numbers, many of the key features are similar in all the cases. In particular, the abduction

| $Re$ | $\overline{C_T}$ | $\overline{C_{Tp}}$ | $\overline{C_{Ts}}$ | $\overline{C_L}$ | $\overline{C_Z}$ | $\eta$ |
|---|---|---|---|---|---|---|
| 6300 | 1.02 | 1.09 | −0.07 | 0.29 | −0.26 | 0.53 |
| 1440 | 0.74 | 0.84 | −0.10 | 0.31 | −0.26 | 0.48 |
| 540 | 0.47 | 0.66 | −0.19 | 0.35 | −0.25 | 0.45 |

TABLE 3. Effect of Reynolds number on fin performance for the POD Mode 1 + 2 + 3 gait at $St = 0.54$.

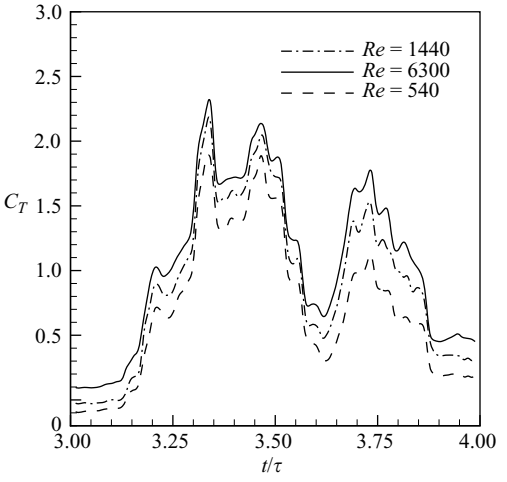


FIGURE 16. Time variation of thrust coefficient at three different Reynolds numbers for the POD Mode 1 + 2 + 3 gait and $St = 0.54$.

and adduction tip vortices, as well as the adduction ventral-leading-edge vortex, are clearly visible in all cases. Reduction in the Reynolds number, however, does tend to dissipate the adduction dorsal-edge vortex as it does many of the smaller scale vortex structures. It is also noted that as the Reynolds number decreases, the helical structure of the abduction tip vortex becomes less noticeable.

Figure 16 shows the variation of the forces on the fin for the three Reynolds numbers, and table 3 shows the mean values of the force coefficients for the three force components. We focus here on the pressure forces (denoted by $C_{Tp}$ in table 3) in order to examine how the reduction in the Reynolds numbers and the associated changes in the vortex structures affect the pressure component of the thrust on the fin. The shear stress component ($C_{Ts}$) is quite small at these Reynolds numbers, and as expected, the shear drag increases with decreasing Reynolds number. The plots and the table essentially indicate that there is relatively little change in the pressure forces as the Reynolds numbers is reduced from 6300 to 1440. As the Reynolds number is reduced further to 540, there is some reduction in the force magnitude. The reduction is most noticeable during the adduction phase, where the peak force coefficient drops from about 1.7 for $Re = 6300$ to 1.1 for $Re = 540$. The changes in the other force coefficients are even smaller in magnitude, and these figures are not shown here.

Table 3 shows that there is about a 20 % loss of pressure thrust when the Reynolds number is reduced to 1140, and this loss increases to about 40 % as the Reynolds number is reduced to 540 from 6300. On the other hand, time-averaged lift forces

increase slightly with decrease in Reynolds number, whereas the spanwise force coefficients remain unchanged for three cases. As a result, the efficiency value of 0.53 calculated for $Re = 6300$ drops to 0.48 and 0.45 for the $Re = 1440$ and $Re = 540$ cases, respectively.

The above analysis of the vortex structures and forces indicates that indeed, as the Reynolds number is reduced by a factor of about 10, some fine-scale vortex structures are dissipated rapidly, and there is a significant (40 %) reduction in the forces produced by the fin. At the same time, the general similarity in the vortex topology and temporal variation of the forces indicates that the essential fluid dynamic mechanisms are unchanged within the range of Reynolds numbers studied here. This is in line with past studies (Dong *et al.* 2006) of rigid flapping foils that have also found little qualitative change in these flows as the Reynolds numbers is changed from 100 to 400. Anderson *et al.* (1998) have also noted the insensitivity of the qualitative features of the flows associated with flapping foils for Reynolds numbers ranging from $O(10^3)$ to $O(10^4)$. The fin performance at Reynolds numbers much higher than 6300 is, however, unknown and, given the CPU cost of such simulations, cannot be easily assessed using numerical simulations.

The Reynolds-number-scaling effect studies suggest that further performance analysis can be carried out at a Reynolds number of 1440, which is about one fourth of the nominal value. An advantage of studying this lower Reynolds number is that it requires 2.35 million points, instead of the 4.9 million employed for high-Reynolds-number simulation. This saves significant CPU time and allows for more rapid assessment of the scaling effects.

## 7. Strouhal-number-scaling effects

In this section, the effect of Strouhal number on the fin performance is examined. In flapping-foil fluid mechanics and aquatic locomotion, the Strouhal number is considered a key parameter, one which has a significant effect on the wake characteristics and propulsive performance. The Strouhal number for flapping foils is typically defined as $St = L_w f/U_\infty$, where $L_w$ is a measure of width of the wake of the foil. For a pitching heaving foil, the wake width is well characterized by the the total (peak-to-peak) heave amplitude of the foil (Triantafyllou *et al.* 1992). Some studies of pitching–rolling foils have used the total amplitude at 70 % span to characterize the wake width (Triantafyllou, Techet & Hover 2004; Techet *et al.* 2005). If the current pectoral fin is assumed to be similar to a pitching–rolling foil, then based on the 70 % span amplitude definition, the Strouhal number for the current case would be about 0.36. It should be noted that the kinematics of fish swimming at a variety of speeds with their pectoral fins have been studied by several authors, and scaling relationships have been determined for surfperch, a species that has a body shape and pectoral fin locomotor mode very similar to the sunfish modelled in this paper. For these fish, increases in swimming speed with the pectoral fins are accomplished primarily through changes in frequency of pectoral fin beats (Gibb, Jayne & Lauder 1994; Drucker 1996; Drucker & Jensen 1996). Thus, changing the Strouhal number while maintaining the same fin kinematics allows us to examine the effect of change in fin frequency and speed for these fish as well as for underwater vehicles inspired by such fish.

Freymuth (1990) and Triantafyllou, Triantafyllou & Gopalkrishnan (1991) have also shown that pitching–heaving foils operating at Strouhal numbers in the vicinity of about 0.25 produce the so-called inverse Kármán vortex street and that the

| $St$ | $\overline{C_T}$ | $\overline{C_L}$ | $\overline{C_Z}$ | $\eta$ |
|---|---|---|---|---|
| 0.41 | 0.59 | 0.30 | −0.23 | 0.37 |
| 0.54 | 0.74 | 0.32 | −0.26 | 0.48 |
| 0.70 | 0.92 | 0.33 | −0.27 | 0.29 |

TABLE 4. Effect of Strouhal number on fin propulsive performance for the POD Mode $1 + 2 + 3$ gait at $Re = 1440$.

propulsive efficiency is highest at these Strouhal numbers. For pitching–heaving foils of finite aspect ratio, the wake shows a vortex structure that is characterized by interlinked vortex loops and oblique wakes (Dong *et al.* 2006). Furthermore, the optimal Strouhal number is found to be a function of both the foil aspect ratio and Reynolds number (Dong *et al.* 2006). Studies by Triantafyllou, Hover & Licht (2003) have shown that fish and mammals that use caudal fin propulsion generally swim in a range of Strouhal numbers from about 0.25 to 0.35, and this tends to confirm the optimality of this Strouhal number for caudal-fin-based propulsion. A more recent study of propulsion in odontocete cetaceans (Rohr & Fish 2004) suggests a Strouhal number range of 0.2–0.3.

To our knowledge, the correlation of Strouhal number with propulsive performance for pectoral-fin-based (labriform) propulsion has not yet been explored extensively. Pectoral fins of fish that employ them in a labriform mode of propulsion are highly complex and varied in shape and also undergo varying degrees of deformation. It is therefore more difficult to parameterize the kinematics for this mode, and this is perhaps one reason why the such investigations of labriform propulsion have not been carried out. The only work on this topic is by Walker & Westneat (2000) who examined labriform propulsion for a model based on the bird wrasse (*Gomphosus varius*) pectoral fin. Their study, which employed a relatively elaborate blade-element model, indicated a maximum efficiency for a 'flapping stroke' of about 58 %, and this occurred at a Strouhal number (based on fin-tip amplitude at 70 % span) of about 0.16.

In the current study, we simulate two additional cases that cover a relatively wide range of Strouhal numbers around the nominal value of 0.54. In particular, we simulate two cases with Strouhal numbers of 0.41 and 0.70 while keeping the Reynolds number constant at 1140. These represent a +30 % and −24 % variation over the nominal value of the Strouhal number. Note also that all these cases are for the Mode 1+2+3 case which we have identified as a case of interest for a biorobotic pectoral fin. Table 4 shows the parameters for the various cases in described in this section.

The wake structure at the end of the fin-beat cycle for the $St = 0.41$ and 0.70 cases are shown in figure 17, and these can be compared with the corresponding plot for the nominal $St = 0.54$ case in figure 15($b$). Similarities can be seen in the wake structures for all cases, although we note that the abduction tip vortex gets stronger as the Strouhal number is increased. It is also noted that this vortex detaches from the fin at the end of the cycle for the lower-Strouhal-number case. A decrease (increase) in Strouhal number implies a decrease (increase) in the fin-tip velocity relative to the flow velocity, and this explains the increase in the strength of the tip vortex with increasing Strouhal number. Viewing the Strouhal number as a ratio of the convective time scale to the fin flapping time scale, a decrease in Strouhal number

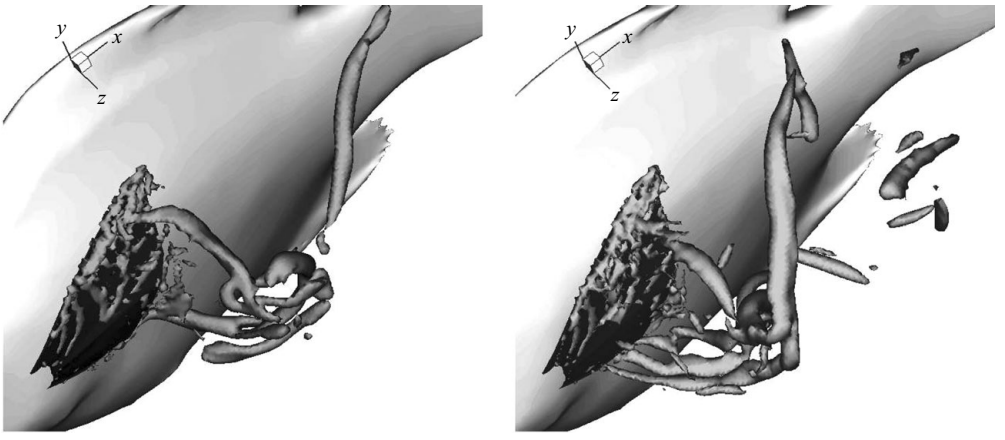


(*a*) $St = 0.41$ (*b*) $St = 0.70$

FIGURE 17. Wake structures for the Mode 1+2+3 gait at $Re = 1440$ at two different Strouhal numbers.

implies an increase in the flapping time scale, which allows vortex structures such as the abduction tip vortex to convect farther downstream during the fin stroke and detach from the adduction vortices.

Figure 18 shows the time variation of the force coefficient on the fin. The key point to note is that the hydrodynamic performance of the fin is found to be quite sensitive to the Strouhal number, and the magnitudes of all the force components increase with increasing Strouhal number. It is however interesting to note that of all the force components, the thrust component is the most sensitive to changes in Strouhal number. As expected, the high-frequency case produces more thrust, and the time-averaged values in table 4 show that 24 % more thrust is produced when the Strouhal number is increased from 0.54 to 0.7. On the other hand, there is about a 20 % reduction in the mean thrust when the Strouhal number is decreased to 0.41. The time-averaged values of lift and spanwise forces do not show similar changes, firstly since they exhibit lower sensitivity to $St$ and secondly due to the fact that negative and positive values during the two phases of the cycle effectively cancel out the net forces in all the cases. The general trend of increase in the thrust coefficient with Strouhal number is in line with data on rigid flapping foils (Anderson *et al.* 1998; Dong *et al.* 2006).

Table 4 also shows the computed propulsive efficiency for all the cases, and these reveal a very interesting result. The simulations indicate that the $St = 0.54$ case is indeed the most efficient case with an efficiency of 48 %. As the Strouhal number is increased to 0.70, there is a significant decline in efficiency to 29 %. Thus, although the higher-Strouhal-number case produces more thrust, it does so with a significantly reduced propulsive efficiency. There is also a reduction in the efficiency to 37 % as the Strouhal number is reduced to 0.41, but this decrease is clearly not as precipitous as that seen at the higher Strouhal number. The current simulations therefore suggest that there is an optimal Strouhal number range for this highly deformable pectoral fin and that the fish indeed operates in this optimal range. The fact that the optimal Strouhal value of 0.54 is higher than the 0.25 value predicted in previous studies (Triantafyllou, Triantafyllou & Grosenbaugh 1993; Rohr & Fish 2004) is not surprising, since pectoral fin propulsion is expected to have significantly different fluid dynamics than caudal fin propulsion which was the focus of these previous studies. Furthermore, the

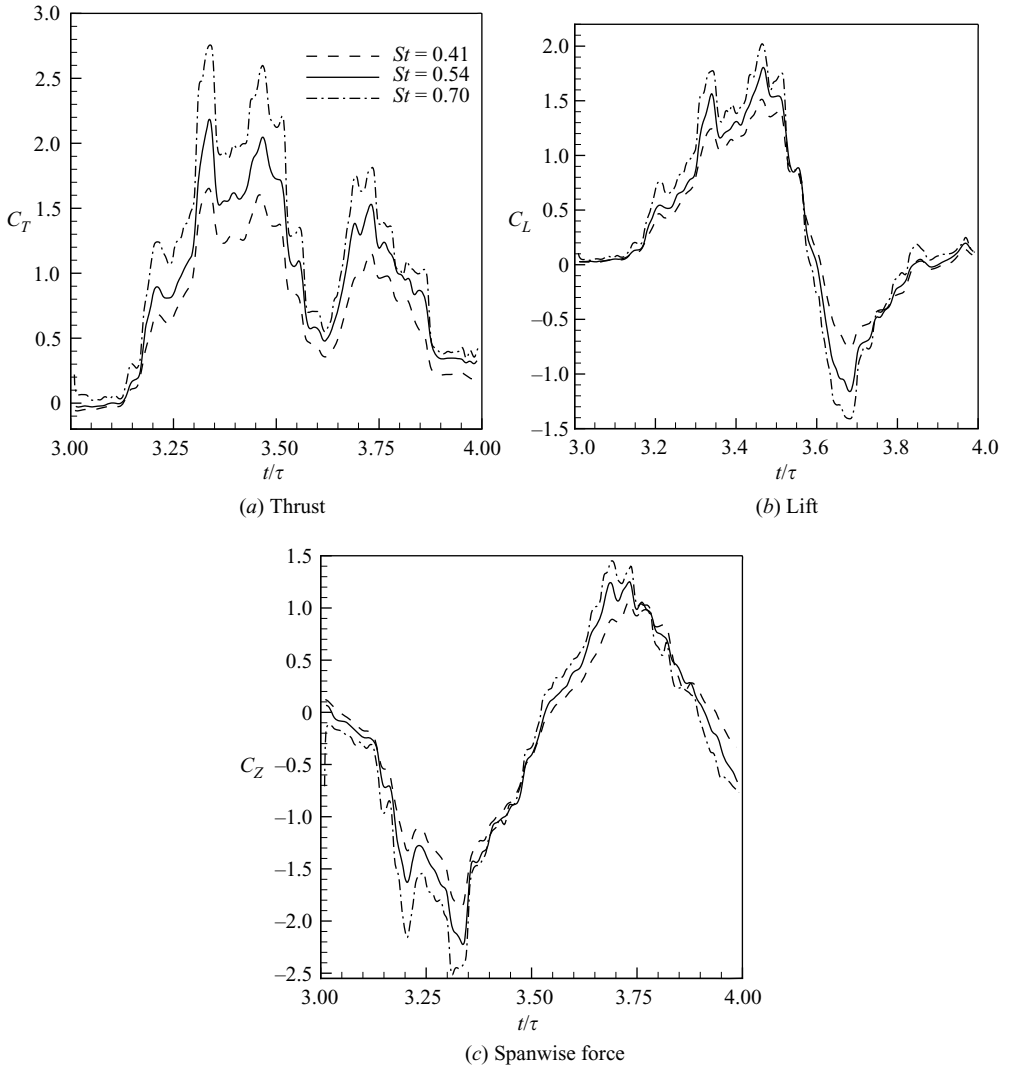


FIGURE 18. Time variation of force coefficients at three different Strouhal numbers for $Re = 1440$.

so-called optimal range depends very much on the precise definition of the Strouhal number. In fact, as pointed out above, if we choose a definition of the Strouhal number that is in line with that used for pitching–rolling foils (Techet *et al.* 2005), then the Strouhal number of the current fin is about 0.36 which is close to the upper end of the optimal range indicated by Triantafyllou *et al.* (1993).

## 8. Fin performance for a starting manoeuvre

In addition to the above two cases, we simulate a case of the fin operating in a stationary flow. From a practical point of view, this simulation models the situation of a fish (or a biorobotic vehicle with similar fins), employing this fin stroke for a 'starting' manoeuvre. Such a case is characterized by the Stokes (or reduced) frequency defined as $S = fL_{fin}^2/\nu$. Note that for cases with crossflow, $S = St \times Re$, and therefore

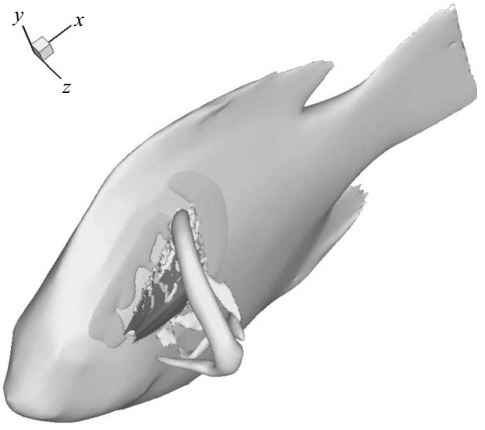


FIGURE 19. Wake structures for the Mode 1+2+3 gait for the stationary ($St = \infty$) case.

$S$ is not an independent non-dimensional parameter. In fact, although we have chosen Strouhal and Reynolds numbers as the primary non-dimensional parameters in the current study, we could equally well have chosen the Strouhal and Stokes numbers as the two independent non-dimensional parameters. For the nominal case with $St = 0.54$ and $Re = 1140$, the Stokes frequency is equal to 616, and we keep the same value of Stokes frequency for the stationary flow case in order to ensure that only one parameter is different from the nominal case. Note that for this stationary flow case, the Strouhal number tends to infinity and the Reynolds number to zero.

Figure 19 shows the vortex structures for the starting manoeuvre case at the end of the fin stroke. Not surprisingly, the absence of the crossflow results in a vortex topology which is markedly different from the other case. The flow at the end of the stroke is characterized by a single vortex structure that tracks the trajectory of the fin tip and is made up of the adduction tip vortex and a vortex shed from the dorsal edge during adduction.

Finally, we examine the force production for the starting manoeuvre case. In order to compare the performance of this case with the nominal case, we redefine the force coefficients using the fin-tip velocity ($V_{tip}$) as the velocity scale. Note that this is necessitated by the fact that $U_\infty$ is zero for the starting manoeuvre case. Thus, we define a new thrust coefficient as

$$C'_T = \frac{T}{\frac{1}{2}\rho V_{tip}^2 A_{fin}}, \tag{8.1}$$

where $V_{tip}$ is estimated simply as $\pi f D_{tip}$. For the nominal case, this implies that $V_{tip}/U_\infty = \pi St(D_{tip}/L_{fin})$ and, furthermore, $C'_T = C_T \times (U_\infty^2/V_{tip}^2)$.

In figure 20, we have plotted the thrust force coefficients for the nominal case as well as the starting manoeuvre case. We focus here on the pressure thrust in order to eliminate from consideration the effect of viscous drag which is significant for the starting manoeuvre. As can be seen from this plot, the fin fails to produce any significant magnitude of pressure thrust during the starting manoeuvre. The mean value of thrust coefficient $C'_{Tp}$ for the starting manoeuvre case is 0.05 which is about 16 % of value for the nominal case, which is 0.33. Force production in the lateral directions is similarly small.

The inability of the fin to produce any appreciable force during this starting manoeuvre is quite striking. The implication of this for both the fish locomotion and

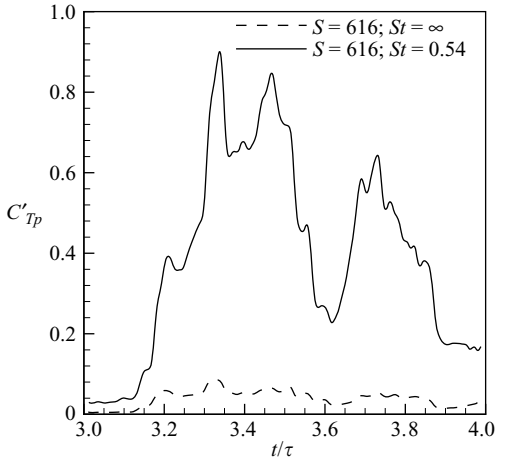


FIGURE 20. Time variation of force coefficients due to pressure for the nominal and starting manoeuvre cases.

a biorobotic fin design is that the fin kinematics that are the basis of the current study are appropriate only for a cruise-type condition, where the fish/vehicle is moving forward at some appreciable speed. In particular, this fin stroke is inappropriate for use in starting manoeuvres in which the fish/vehicle attempts to accelerate from zero initial speed, since this fin stroke will produce very little thrust when the forward speed is zero (or very small). In fact, it is well known that many labrids employ a very different 'paddling-type' stroke (Walker & Westneat 2002*a*,*b*) to initiate forward motion and then transition to a 'flapping" stroke as the forward speed increases. The current simulations would seem to provide a clear and quantitative reason as to why this behaviour is well justified. Our results also indicate that for an underwater vehicle that would use similar fin-inspired propulsors, starting manoeuvres using this kind of a fin stroke would be very slow and inefficient.

## 9. Conclusions

POD has been used to study the kinematics and fluid dynamics of pectoral fin propulsion in a bluegill sunfish. The pectoral fin of this fish exhibits complex kinematics coupled with a high degree of deformation, and POD allows us to separate the motion into distinct components that are amenable to further study. The POD analysis shows that despite the seeming complexity of the fin kinematics, the fin motion is dominated by a relatively small number of orthogonal modes. The first three modes capture about 67 % of the total motion, whereas the first five modes account for 80 % of the fin gait. The first three modes are found to have very distinct and identifiable characteristics: Mode 1 involves considerable movement away from the body in what we call the 'cupping' motion, where the fin cups forward as it is abducted. It leads to a rapid acceleration of the fin dorsal and ventral edges, forming two leading edges from them. Mode 2 is named an 'expansion' mode in which the fin expands to present a larger surface area during adduction. Mode 3 is a wave-like motion in the spanwise direction, which occurs along the dorsal edge of the fin. It involves a rapid spanwise 'flick' of the fin tip along the dorsal edge of the fin during the abduction phase. In contrast to Modes 1 and 2, which result from active angular

motion of the fin rays by the fish, Mode 3 is primarily a result of flow-induced deformation.

In order to understand the role that each of the dominant modes plays in determining the propulsive performance of the fin, we synthesize low-dimensional gaits from the POD modes and subject them to flow simulations using a sharp-interface immersed-boundary Navier–Stokes solver. These simulations indicate that a gait synthesized from just the first three modes recovers 92 % of the thrust of the pectoral fin. Thus, from the point of view of bio-inspired design, a fin propulsor that produces these three modes would lead to an effective design.

We have also used numerical simulations to examine how the performance of the fin scales with the Reynolds and Strouhal numbers. Simulations indicate that as the Reynolds number is reduced by about an order of magnitude from the nominal value of 6300, the mean thrust due to pressure reduces by about 40 %. The propulsive efficiency also reduces monotonically with Reynolds number and drops by about 15 % as the Reynolds number is reduced about an order of magnitude. However, the simulations indicate that there is no distinct change in the flow mechanisms or the vortex topology despite this large decrease in Reynolds number. This indicates that the pectoral fin kinematics adopted by the fish would be effective over a relatively large range of spatial scales.

The performance of the fin is found to be much more sensitive to the Strouhal number. The thrust coefficient is found to increase monotonically with Strouhal number and shows about a 21 % increase as the Strouhal number is increased from 0.54 to 0.71 and about an 18 % decrease as the Strouhal number is decreased to 0.41. Interestingly, the current simulations suggest that a Strouhal number of 0.54, which is the nominal value for the fish in the current study, results in the highest propulsive efficiency. This suggests that the fish swims in an optimal range of this parameter. The presence of an optimal range, although well-known for caudal fin propulsion and engineered flapping foils, is not well-established for pectoral fin propulsion. The current simulations indicate that such a range does exist. Finally, a simulation of a 'starting' manoeuvre in which the free stream velocity is reduced to zero while keeping the same fin kinematics shows that the fin kinematics adopted by the fish during cruise is not well suited for accelerating from a stationary position.

The current POD approach coupled with computational fluid modelling therefore provides a useful means of gaining insight into the fluid dynamics of pectoral fin motion, where the pectoral fin undergoes large changes in shape due to passive and active deformation. These insights help us better understand the functional morphology of pectoral fins and are also helping us design biomimetic flapping fin propulsors (Tangorra *et al.* 2007).

This research was funded by the ONR MURI grant N00014-03-1-0897. Detailed comments from one of the anonymous reviewers were very helpful.

## REFERENCES

Alexa, M. & Mueller, W. 2000 Representing animations by principal components. *Eurographics* **19**, 411–418.

Anderson, J. M., Streitlien, K., Barrett, D. S. & Triantafyllou, M. S. 1998 Oscillating foils of high propulsive efficiency. *J. Fluid Mech.* **360**, 41–72.

Barber, T. J., Ahmed, M. H. & Shafi, N. A. 2005 POD snapshot data reduction for periodic flows. In *Proceedings of 43th Aerospace Sciences and Meeting Exhibit*. Reno, NV.

Berkooz, G, Holmes, P. & Lumley, J. L. 1993 The proper orthogonal decomposition in the analysis of turbulent flows. *Annu. Rev. Fluid Mech.* **25**, 539–75.

Bozkurttas, M. 2007 Hydrodynamic performance of fish pectoral fins with application to autonomous underwater vehicles. PhD thesis, The George Washington University, Washington, DC.

Bozkurttas, M., Dong, H., Mittal, R., Lauder, G. V. & Madden, P. 2006 Hydrodynamic performance of deformable fish fins and flapping foils. *Paper* 2005-1392. AIAA.

Dong, H., Bozkurttas, M., Mittal, R., Madden, P. & Lauder, G. V. 2009 Computational modelling and analysis of the hydrodynamics of a highly deformable fish pectoral fin. *J. Fluid Mech.* submitted February 2009.

Dong, H., Mittal, R. & Najjar, F. M. 2006 Wake topology and hydrodynamic performance of low aspect-ratio flapping foils. *J. Fluid Mech.* **566**, 309–343.

Drucker, E. G. 1996 The use of gait transition speed in comparative studies of fish locomotion. *Amer. Zool.* **36**, 555–566.

Drucker, E. G. & Jensen, J. 1996 Pectoral fin locomotion in the striped surfperch. Part 1. Kinematic effects of swimming speed and body size. *J. Exp. Biol.* **199**, 2235–2242.

Drucker, E. G. & Lauder, G. V. 2000 A hydrodynamic analysis of fish swimming speed: Wake structures and locomotor force in slow and fast labriform swimmer. *J. Exp. Biol.* **203**, 2379–2393.

Freymuth, P. 1990 Thrust generation by an airfoil in hover modes. *Exp. Fluids.* **9**, 17–24.

Gibb, A., Jayne, B. C. & Lauder, G. V. 1994 Kinematics of pectoral fin locomotion in the bluegill sunfish lepomis macrochirus. *J. Exp. Biol.* **189**, 133–161.

Hartley, R. & Zisserman, A. 2004 *Multiole View Geometry in Computer Vision*, 2nd edn. Cambridge University Press.

Jayne, B. C., Lozada, A. & Lauder, G. V. 1996 Function of the dorsal fin in bluegill sunfish: motor patterns during four distinct locomotor behaviours. *J. Morphol.* **228**, 307–326.

Kato, N. & Furushima, M. 1996 Pectoral fin model for maneuver of underwater vehicles. In *Proceedings of 14th International Symposium on Unmanned Untethered Submersible Technology*, Durham, NH.

Lauder, G. V. & Madden, P. 2006 Learning from fish: Kinematics and experimental hydrodynamics for roboticists. *Intl J. Automat. Comput.* **3** (4), 325–335.

Lauder, G. V., Madden, P., Hunter, I., Tangorra, J., Davidson, N., Proctor, L., Mittal, R., Dong, H. & Bozkurttas, M. 2005 Design and performance of a fish fin-like propulsor for AUVs. In *Proceedings of 14th International Symposium on Unmanned Untethered Submersible Technology*, Durham, NH.

Lauder, G. V., Madden, P., Mittal, R., Dong, H. & Bozkurttas, M. 2006 Locomotion with flexible propulsors. Part 1. Experimental analysis of pectoral fin swimming in sunfish. *Bioinsp. Biomimet.* **1**, S25–S34.

Liang, Y. C., Lee, H. P., Lim, S. P ., Lin, W. Z., Lee, K. H. & Wu, C. G. 2002 Proper orthogonal decomposition and its applications. Part 1. Theory. *J. Sound Vib.* **252** (3), 527–544.

Lighthill, J. 1975 *Mathematical Biofluiddynamics*. SIAM.

Mittal, R., Dong, H., Bozkurttas, M., Lauder, G. V. & Madden, P. 2006 Locomotion with flexible propulsors. Part 2. Computational modelling of pectoral fin swimming in a sunfish. *Bioinsp. Biomim.* **1**, S35–S41.

Mittal, R., Dong, H., Bozkurttas, M., Najjar, F., Vargas, A. & von Loebbecke, A. 2008 A versatile immersed boundary method for incompressible flows with complex boundaries. *J. Comp. Phys.* **227**, 4825–4852.

Mittal, R. & Iaccarino, G. 2005 Immersed boundary methods. *Annu. Rev. Fluid Mech.* **37**, 239–261.

Ramamurti, R., Sandberg, W. C., Lohner, R., Walker, J. A. & Westneat, M. W. 2002 Fluid dynamics of flapping aquatic flight in the bird wrasse: three-dimensional unsteady computations with fin deformation. *J. Exp. Biol.* **205** (10), 2997–3008.

Ramamurti, R., Sandberg, W., Ratna, B., Naciri, J. & Spilman, C. 2005 3-d unsteady computational investigations of the effect of fin deformation on force production in fishes. In *Proceedings of 14th International Symposium on Unmanned Untethered Submersible Technology*, Durham, NH.

Rohr, J. J. & Fish, F. E 2004 Strouhal numbers and optimization of swimming by odontocete cetaceans. *J. Exp. Biol.* **207**, 1633–1642.

Soria, J. & Cantwell, B. J. 1993 Identification and classification of topological structures in free shear flows. In *Eddy Structure Identification in Free Turbulent Shear Flows* (ed. J. P. Bonnet & M. N. Glauser), pp. 379–390. Academic.

Standen, E. M. & Lauder, G. V. 2005 Dorsal and anal fin function in bluegill sunfish (*Lepomis macrochirus*): three-dimensional kinematics during propulsion and maneuvering. *J. Exp. Biol.* **205**, 2753–2763.

Tangorra, J. L., Davidson, S. N., Hunter, I. W., Madden, P. G. A., Lauder, G. V., Dong, H., Bozkurttas, M. & Mittal, R. 2007 The development of a biologically inspired propulsor for unmanned underwater vehicles. *IEEE J. Ocean. Engng* **32** (3), 533–550.

Techet, A. H., Lim, K. L., Hover, F. S. & Triantafylou, M. S. 2005 Hydrodynamic performance of a biologically inspired 3D flapping foil. In *Proceedings of 14th International Symposium on Unmanned Untethered Submersible Technology*, Durham, NH.

Triantafyllou, M. S., Hover, F. S. & Licht, S. 2003 The mechanics of force production in flapping foils under steady-state and transient motion conditions. *Tech Rep.* Testing Tank Facility Report 031903. MIT Department of Ocean Engineering.

Triantafyllou, M. S., Techet, A. H. & Hover, F. S. 2004 Review of experimental work in biomimetic foils. *IEEE J. Ocean. Engng* **29**, 585–595.

Triantafyllou, M. S., Triantafyllou, G. S. & Gopalkrishnan, R. 1991 Wake mechanics for thrust generation in oscillating foils. *Phys. Fluids* **3** (12), 2835–2837.

Triantafyllou, G. S., Triantafyllou, M. S. & Grosenbaugh, M. A. 1992 Optimal thrust development in oscillating foils with applications to fish propulsion. *J. Fluids Struct.* **7**, 204–224.

Triantafyllou, M. S., Triantafyllou, G. S. & Grosenbaugh, M. A. 1993 Optimal thrust development in oscillating foils with applications to fish propulsion. *J. Fluids Struct.* **7**, 205–224.

Troje, N. 2000 Decomposing biological locomotion: a framework for analysis and synthesis of human gait patterns. *J. Vision* **2** (5).

Udaykumar, H. S., Mittal, R., Rampunggoon, P. & Khanna, A. 2001 A sharp interface Cartesian grid method for simulating flows with complex moving boundaries. *J. Comput. Phys.* **174**, 345–380.

Urtasun, R., Fua, P., Glardon, P. & Thalmann, D. 2004 Mahalanobis motion generation. *Tech Rep.* IC/2004/13. Swiss Federal Office for Education and Science.

Van-Kan, J. 1986 A second order accurate pressure correction scheme for viscous incompressible flow. *SIAM J. Sci. Stat. Comput.* **7**, 870–891.

Walker, J. A. & Westneat, M. W. 1997 Labriform propulsion in fishes: kinematics of flapping aquatic flight in the bird wrasse, *gomphosus varius* (Labridae). *J. Exp. Biol.* **200**, 1549–1569.

Walker, J. A. & Westneat, M. W. 2000 Mechanical performance of aquatic rowing and flying. *Proc. R. Soc Lond.* B **267**, 1875–1881.

Walker, J. A. & Westneat, M. W. 2002*a* Kinematics, dynamics, and energetics of rowing and flapping propulsion in fishes. *Integr. Compar. Biol.* **42**.

Walker, J. A. & Westneat, M. W. 2002*b* Performance limits of labriform propulsion and correlates with fin shape and motion. *J. Exp. Biol.* **205**, 177–187.

Ye, T., Mittal, R., Udaykumar, H. S. & Shyy, W. 1999 An accurate Cartesian grid method for simulation of viscous incompressible flows with complex immersed boundaries. *J. Comput. Phys.* **156**, 209–240.